

Dark Matter Working Group recommendation for Two Higgs Doublet Model (draft title)

Authorlist to be compiled; Antonio Boveia,^{3,*} Caterina Doglioni,^{8,*} Kristian Hahn,^{14,*} Ulrich Haisch,^{15,16,*} Steven Lowette,²² Tim M.P. Tait,^{25,*}

*DMWG organizers

³Ohio State University, 191 W. Woodruff Avenue Columbus, OH 43210

⁸Fysiska institutionen, Lunds universitet, Lund, Sweden

¹⁴Department of Physics and Astronomy, Northwestern University, Evanston, Illinois 60208, USA

¹⁵Rudolf Peierls Centre for Theoretical Physics, University of Oxford, Oxford, OX1 3PN, United Kingdom

¹⁶CERN, TH Department, CH-1211 Geneva 23, Switzerland

²²Physics Department, Vrije Universiteit Brussel, Brussels, Belgium

²⁵Department of Physics and Astronomy, University of California, Irvine, California 92697, USA

Editor's E-mail: antonio.boveia@cern.ch, caterina.doglioni@cern.ch,
kristian.hahn@cern.ch, ulrich.haisch@physics.ox.ac.uk, ttait@uci.edu

Abstract. Draft abstract.

Contents

1	Model kinematics and mapping to existing models	1
1.1	Description of experimental searches	2
1.1.1	Signatures including a Higgs boson	2
1.1.2	Signatures including a Z boson	2
1.1.3	Signatures including heavy flavor quarks	4
1.2	Kinematic distributions justifying the choice of parameter scan	4
1.2.1	Masses of the A , H , and a bosons (M_A , M_H , and M_a)	4
1.2.2	Mixing angle between the two pseudoscalars A and a ($\sin \theta$)	7
1.2.3	Ratio of the doublet vacuum expectation values ($\tan \beta$)	9
1.2.4	Mass of DM fermion (M_χ)	12
1.3	Comparison with existing pseudoscalar models and recasting of HF+ E_T^{miss} search results	16
2	Parameter grid	19
3	Sensitivity studies	20
3.1	Studies of the $h(bb) + E_T^{\text{miss}}$ signature	20
3.2	Studies of the $Z+E_T^{\text{miss}}$ signature	24
3.3	Sensitivity of other signatures	27
3.3.1	Heavy flavor + E_T^{miss} signatures	27
3.3.2	Jet+ E_T^{miss} signature	27
4	Phenomenological studies of other signatures of 2HDM+a	27
4.0.1	Signatures with $t\bar{t}h + E_T^{\text{miss}}$	28
4.0.2	$tW+E_T^{\text{miss}}$ signature	28
4.0.3	$\bar{t}t$ resonances	29
4.0.4	Four-top final states	31
5	Connection with cosmology	35
5.1	Technical setup	35
5.2	Results	36
6	Conclusions	39
	Appendix	39

1 Model kinematics and mapping to existing models

The signature and kinematic distributions of the 2HDM+a model at colliders are driven by the values assigned to the parameters described in the previous chapter. The model

parameters can affect the total signal cross-section, the kinematic distributions, or both. In order to obtain a representative grid of benchmark points for collider searches and reduce this multi-dimensional parameter space, we scan ranges of the possible values of these parameters and observe the impact on the kinematic distributions for representative collider searches.

In this chapter, we will outline the existing experimental searches that can be used to search for this model, and present the distributions of the kinematic variables for each of the searches as a function of the free parameters of the model. We note that in the following we have chosen to fix the DM coupling y_χ to unity, and $\lambda_{P1} = \lambda_{P2} = \lambda_P = 3$ as explained in ??.

1.1 Description of experimental searches

1.1.1 Signatures including a Higgs boson

Events with a 125 GeV Higgs boson, recently discovered with ATLAS and CMS [1, 2], and E_T^{miss} can indicate the production of Dark Matter candidates that recoil against the Higgs boson [3, 4]. The initial-state radiation (ISR) production of a Higgs boson is suppressed by the small Yukawa couplings of the Higgs boson to light quarks. Thus $h + E_T^{\text{miss}}$ searches such as [5, 6] directly probe potential new interactions of the Higgs and Dark Matter, as predicted by the 2HDM+a model [7, 8] due to the $a - A - h$ vertex.

$h(bb) + E_T^{\text{miss}}$ signature For the case where the Higgs boson decays into two b -quarks, such as studied in [5], the signal kinematics are studied at parton level. This allows a straightforward comparison to the model-independent results in [5], as described in [subsection 3.1](#), and fast iteration over different model scenarios.

1.1.2 Signatures including a Z boson

Events with a Z boson and E_T^{miss} may signal the presence of invisible particles recoiling against the Z boson [9, 10]. LHC searches (e.g. [11, 12] for the most recent ones) have focused on invisible decays of the SM-like Higgs bosons or on topologies where the Z boson is produced as ISR from a quark. The ISR-based topologies generically favor radiation of a gluon or photon rather than a massive gauge boson, thus limiting the discovery sensitivity of a Z-based approach compared to monojet and mono-photon searches. In contrast, the model studied in this document generates the mono-Z signature dominantly via the all-bosonic H-a-Z vertex, which can lead to enhancements in the mono-Z sensitivity compared to jet and photon signatures.

Mono-Z (leptonic) signature Three consecutive stages of event selection are considered in the case the Z decays leptonically:

- Inclusive: Lepton p_T and η requirements corresponding to the typical experimental trigger acceptance are applied.
- Preselection: A dilepton candidate with an invariant mass in a window around the Z mass is required, and a minimum transverse momentum of the $\chi\bar{\chi}$ system is required.

- Final selection: Requirements on the main discriminating variables used in the relevant analyses are added: The angular separation in the transverse plane between the $\chi\bar{\chi}$ and $l^+ l^-$ systems $\Delta\Phi(l, E_T^{\text{miss}})$, the relative transverse momentum difference between them $|p_{T,l} - E_T^{\text{miss}}|/p_{T,l}$ and the angular separation between the leptons $\Delta R(l)$. Additionally, the E_T^{miss} requirement is tightened.

The exact event selection criteria are listed in the appendix, in ???. The results in this and in the following section are at particle level.

Mono-Z (hadronic) signature The hadronic signature in $Z + E_T^{\text{miss}}$ events ($Z \rightarrow q\bar{q}$ decays in association with large missing transverse momentum) is complementary to the leptonic signature. Hadronic decays are more frequent than leptonic decays, but suffer from larger backgrounds. For these reasons, the Z (hadronic) + E_T^{miss} search is favored if the model include higher mass scalar and pseudoscalar bosons.

The event selection in this case changes depending on the production transverse momentum of the Z -boson, as in the case of the exchange of a high-mass CP-even H boson. If the Z -boson is boosted, then its hadronic decay products could be merged into a single jet, and the Z to QCD background discrimination can be improved by exploiting the presence of substructure within a single, large-radius jet (denoted by J). The *boosted* search is performed in addition to the *resolved* search, where the Z decay products are reconstructed as two separate small-radius jets (denoted by j).

For mono- $Z(\rightarrow q\bar{q})$ events intermediated by the exchange of a high-mass CP-even H boson, the Z -boson will be produced with a large transverse momentum and the hadronic decay products of such Z -boson could be merged into a single jet. Such “boosted” event topology is investigated by exploiting the reconstruction technique with a large-radius jet (denoted by J), in addition to more conventional “resolved” event topology where the Z decay products are reconstructed as two separate small-radius jets (denoted by j). The jet reconstruction and the following analysis are all performed at particle level after showering and hadronization implemented in Pythia 8.212 described above.

Two consecutive stages of event selection are considered for the boosted and resolved event topologies:

- Inclusive: minimal kinematic requirements are applied to a pair of small-radius jets (a single large-radius jet) for the resolved (boosted) event topology. These selection criteria are applied separately, i.e, not sequentially.
- Final selection: selection criteria are applied to the a number of variables. The invariant mass of the pair of small-radius jets or the single large-radius jet is required to be within a window around the Z mass. In addition, selection is applied to the azimuthal angular difference between the $\chi\bar{\chi}$ and the hadronic Z -boson system, $\Delta\Phi(jj \text{ or } J, E_T^{\text{miss}})$, and the magnitude of E_T^{miss} . These final selection cuts are applied sequentially to mimic a realistic analysis; in this study the boosted selection cuts are applied first and then the resolved selection cuts are applied to those events that fail the boosted ones.

The exact event selection criteria are listed in the appendix, in ???. The results in this and in the following section are at particle level.

1.1.3 Signatures including heavy flavor quarks

Heavy flavor final state can have sizable contributions to the production of the CP-even and CP-odd scalar mass eigenstates, due to the Yukawa structure of the couplings in the SM sector.

1.2 Kinematic distributions justifying the choice of parameter scan

1.2.1 Masses of the A , H , and a bosons (M_A , M_H , and M_a)

The masses of the mediators M_A , M_H , and M_a of the pseudoscalars A and a and the scalar H , which are the mediators of the resonant mono- h and mono- Z processes, affect the shape of the E_T^{miss} distribution of these processes. In the mono- Z and mono- H channels, the resonant production occurs through the $2 \rightarrow 1 \rightarrow 2$ processes $gg \rightarrow A \rightarrow ah$ and $gg \rightarrow H \rightarrow aZ$, respectively, with the light pseudoscalar decaying invisibly as $a \rightarrow \chi\chi$. In this case, the $A/H \rightarrow ah$ process produces a resonance in the invariant mass distribution of the final state system with a width determined by the widths of a , A/H , and of the SM bosons. This results in a peak in the transverse momentum distribution of the DM system, reconstructed as E_T^{miss} in the detector.

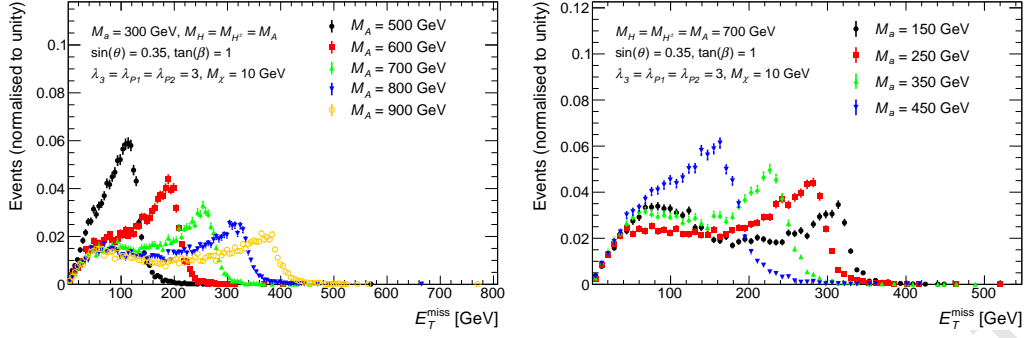
The location of this Jacobian peak can be calculated analytically starting from the masses of the particles involved in the decay [7]:

$$E_T^{\text{miss}, \text{max}} \approx \frac{\sqrt{\left(M_{A/H}^2 - M_a^2 - M_{h/Z}^2\right)^2 - 4M_a^2 M_{h/Z}^2}}{2M_{A/H}}. \quad (1.1)$$

Thus, increasing M_A results in a Jacobian peak at higher E_T^{miss} , as shown in Figure 1a, Figure 2 and Figure 3. Conversely, models with higher M_a have a Jacobian peak at lower E_T^{miss} , as indicated in Figure 1b and Figure 4. For $M_{A/H} \approx M_a + m_{Z/h}$, both the a and Z/h bosons are produced approximately at rest, leading to an event population with overall low boost. These qualitative trends are consistent with the distributions of the other main selection variables as shown in the appendix (??).

A potentially large fraction of the mono- h signal events is also produced in non-resonant $2 \rightarrow 3$ processes $gg \rightarrow h\chi\chi$, as in ??, leading to a broader distribution of the invariant mass of the decay products. Consequently, this results in a broader and softer E_T^{miss} distribution that is distinct from the Jacobian peak discussed above, and contributes to the off-peak features of Figure 1b and Figure 1a.

The masses M_a and M_A influence the kinematics in the $t\bar{t} + E_T^{\text{miss}}$ signature as well. As shown in Figure 5, the E_T^{miss} , and leading and trailing top quark p_T distributions broaden with increasing M_a . Similarly, for values of $M_A < M_a$, as M_A increases, the kinematic distributions mentioned above also broaden, as shown in Figure 6.



(a) E_T^{miss} distribution for points with different M_a and fixed $M_A = 300$ GeV. (b) E_T^{miss} distribution for points with different M_a and fixed $M_A = 700$ GeV.

Figure 1: Parton-level E_T^{miss} distribution of mono-Higgs events for different M_a and M_A , with $M_H = M_{H^\pm} = M_A$, $\sin \theta = 0.35$, $\tan \beta = 1$, $M_\chi = 10$ GeV and $\lambda_{P1} = \lambda_{P2} = \lambda_3 = 3$

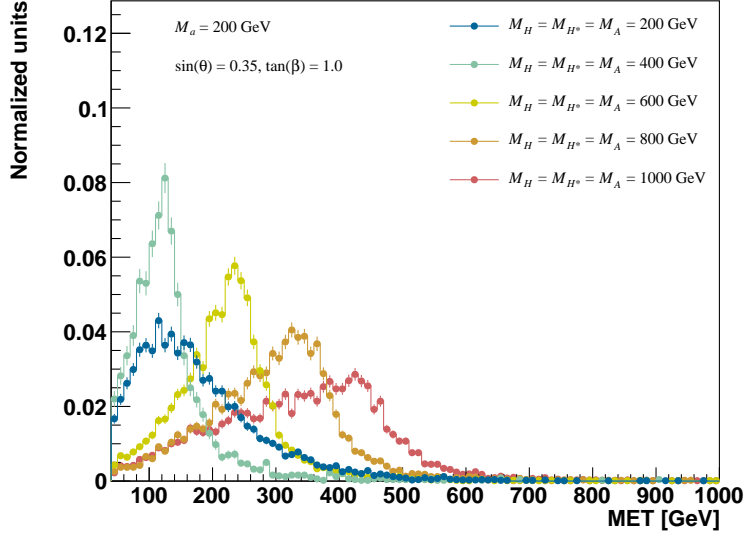


Figure 2: The E_T^{miss} distribution in signatures including a Z boson after preselection in the leptonic channel, with varying M_H values for fixed $M_a = 200$ GeV and $M_A = M_{H^\pm} = M_H$.

Since the shape of the E_T^{miss} distribution affects the design of experimental searches, and to a large extent their sensitivity, *it is desirable to scan the M_A and M_a parameter space.*

In designing a search for evidence of this particular model, it may be useful to consider not only the E_T^{miss} , but also the transverse mass M_T^1 variable. The distributions of both variables after final selection are shown in Figure 7 for the $Z + E_T^{\text{miss}}$ searches. Both distributions show Jacobian peak structures due to dominant effect of the diagram with

¹The massless definition is used here: $M_T = \sqrt{2E_T^{\text{miss}} p_{T,Z} (1 - \cos(\Delta\phi))}$

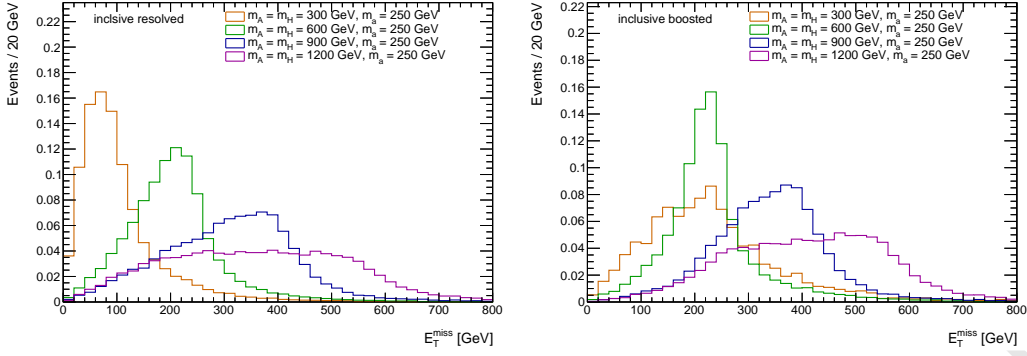


Figure 3: E_T^{miss} distributions in the resolved (left) and boosted (right) hadronic Z search, after applying the inclusive selection. The signal masses are chosen to be $M_H = 300, 600, 900$ and 1200 GeV with the fixed $M_a = 250$ GeV and $M_A = M_{H^\pm} = M_H$.

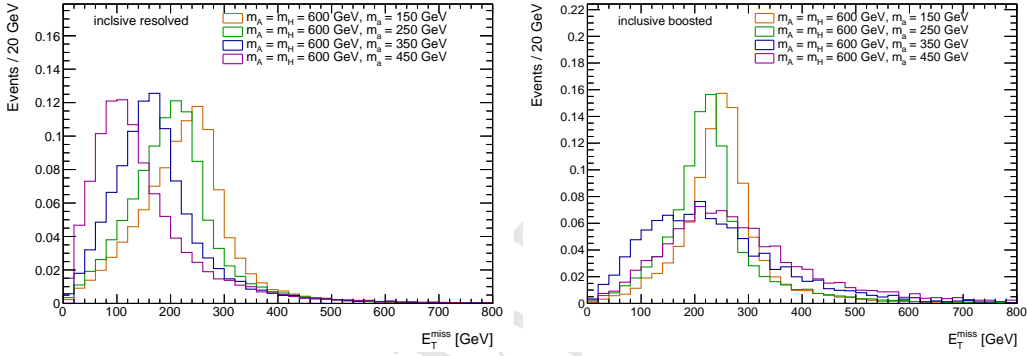


Figure 4: E_T^{miss} distributions in the resolved (left) and boosted (right) hadronic Z search, after applying the inclusive selection. The signal masses are chosen to be $M_a = 150, 250, 350$ and 450 GeV with the fixed $M_H = 600$ GeV ($= M_A = M_{H^\pm}$).

resonant H exchange. In the case of $M_a < M_H$, the peak structure is more defined in the M_T distribution than in the E_T^{miss} , thus helping to distinguish a possible signal from background. Where the resonant diagram does not contribute, i.e. for $M_a \approx M_H$ or $M_a > M_H$, the M_T distribution does not show a significantly different structure from the E_T^{miss} distribution and will not provide an improved sensitivity.

For mono- h , the **mass of the heavy neutral scalar Higgs boson H** has an indirect effect on the rate and kinematics of the signal. This is caused by the dependence of the coupling strength of the $a - A - h$ vertex, and thus decay width of the pseudoscalar A , on M_H [7]. Therefore, a change of M_H can strongly affect the relative contribution of resonant versus non-resonant signal processes, as illustrated in Figure 8. For mono- Z , there is no corresponding effect of M_A on the resonant and non-resonant signal yields, since the $a - H - h$ vertex has a simpler structure with no M_A dependence.

The choice $M_H = M_A$ results in a detectable total cross section and a dominant contribution of the resonant mono- h signal process for many signal points. This choice allows

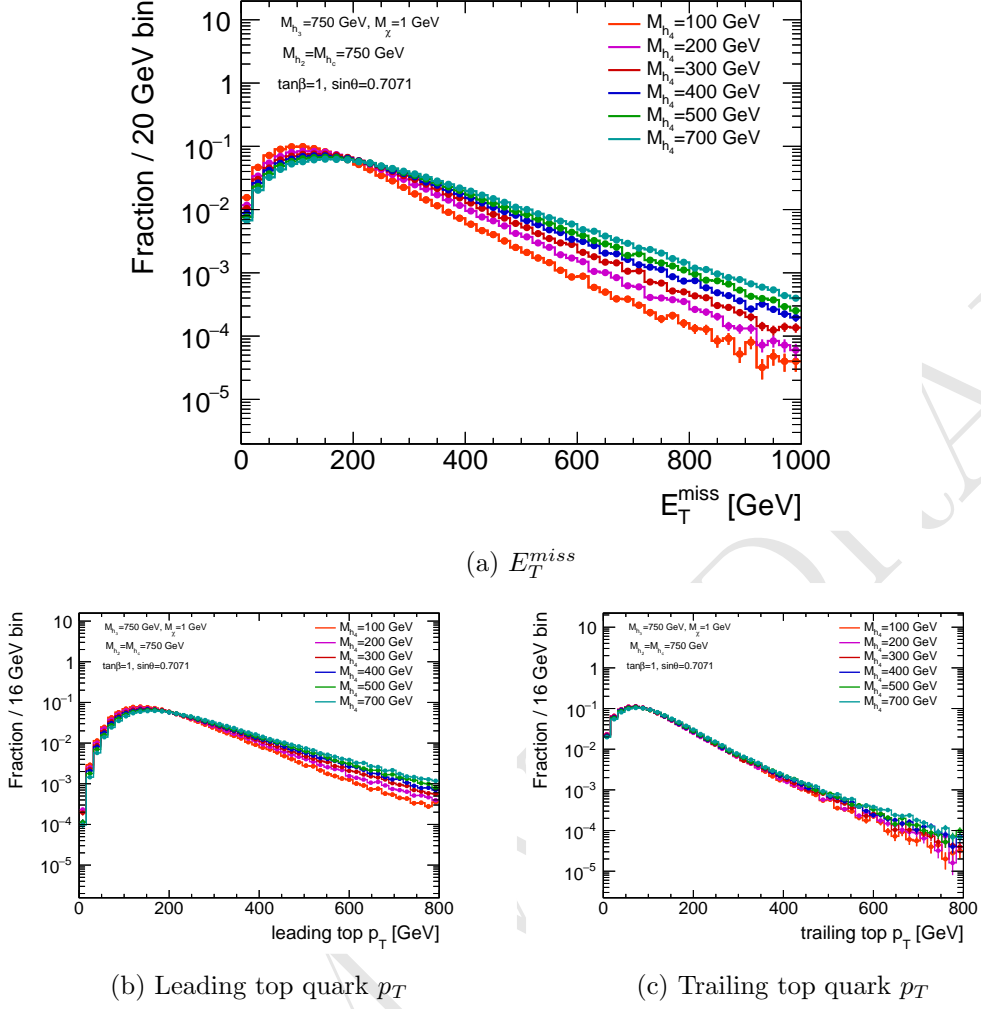


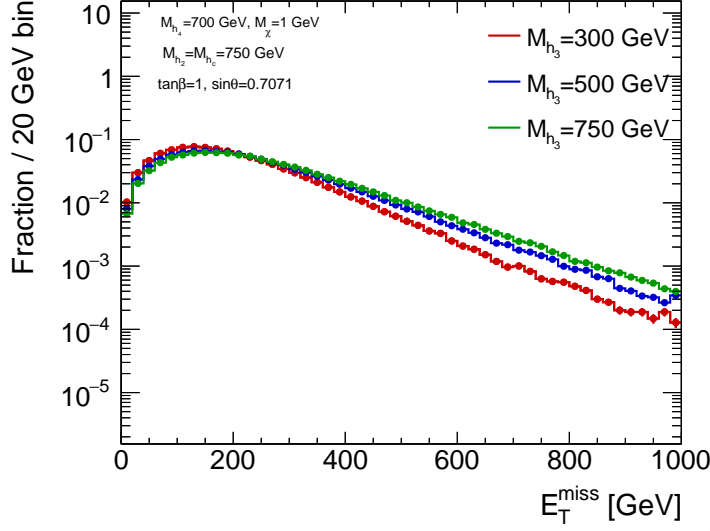
Figure 5: The E_T^{miss} , leading and trailing top p_T distributions for inclusive $t\bar{t} + \chi\bar{\chi}$ production for various values of M_A , with $M_A = 750$ GeV, $M_H = M_{H^\pm} = 750$ GeV, $\tan\beta = 1$, and $\sin\theta = 0.7071$.

us to test diverse E_T^{miss} distributions and results in about equal contributions to the sensitivity through the $Z + E_T^{\text{miss}}$ and $h + E_T^{\text{miss}}$ signatures, highlighting their complementarity. For this reason *the choice $M_H = M_A$ is adopted for all scans.*

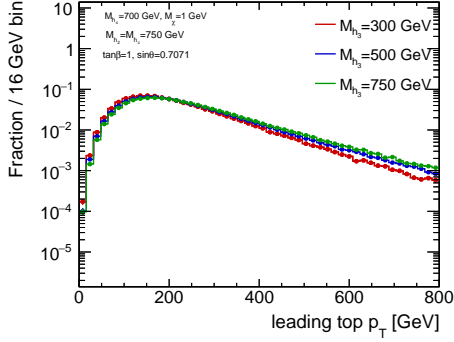
The mass of the neutral scalar H^\pm does not affect the model kinematics, as shown in Appendix ???. Models with $M_{H^\pm} \neq M_H$ are moreover strongly constrained by electroweak precision measurements of the ρ parameter [7]. Therefore, for simplicity, the *neutral scalar H^\pm is assumed to be mass-degenerate to H .*

1.2.2 Mixing angle between the two pseudoscalars A and a ($\sin\theta$)

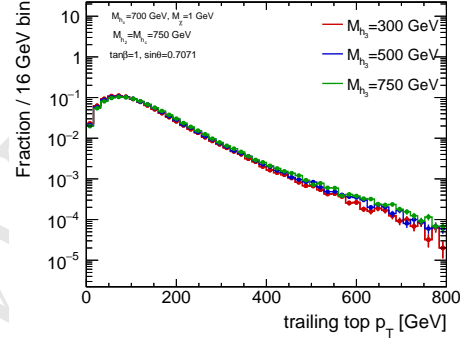
The sine of the mixing angle between the two pseudoscalars A and a , $\sin\theta$, affects not only the cross section, but also the shape of the E_T^{miss} distribution in searches including a



(a) E_T^{miss}



(b) Leading top p_T



(c) Trailing top p_T

Figure 6: The E_T^{miss} , leading and trailing top p_T distributions for inclusive $t\bar{t} + \chi\bar{\chi}$ production for various values of M_A , with $M_a = 700$ GeV, $M_H = M_{H^\pm} = 750$ GeV, $\tan \beta = 1$, and $\sin \theta = 0.7071$, before any analysis selection.

Higgs boson, as shown in Figure 12a. For the resonant diagram $gg \rightarrow A \rightarrow ah \rightarrow \chi\bar{\chi}h$, the product of cross section times branching ratios $\mathcal{B}(A \rightarrow ah)\mathcal{B}(a \rightarrow \chi\bar{\chi})$ scales with $\sin^2 \theta \cos^6 \theta$, while for the diagram $gg \rightarrow a \rightarrow A^*h \rightarrow \chi\bar{\chi}h$, the product of cross section times branching ratios $\mathcal{B}(a \rightarrow Ah)\mathcal{B}(A \rightarrow \chi\bar{\chi})$ scales with $\sin^6 \theta \cos^2 \theta$. This is shown in Appendix ???. Therefore, at small $\sin \theta$, the resonant diagram $A \rightarrow ah$ is the dominant production mode and the E_T^{miss} distribution has a Jacobian peak following Equation 1.1; while at large $\sin \theta$, the $a \rightarrow A^*h$ diagram starts to dominate and produces a second peak at a lower E_T^{miss} value.

Scans of the $\sin \theta$ parameter show they have minimal effect on the kinematic distributions for searches with a Z boson (Figure 12b).

In the $t\bar{t} + E_T^{\text{miss}}$ signature, the A (h_3 in the figure) and a (h_4 in the figure) mass

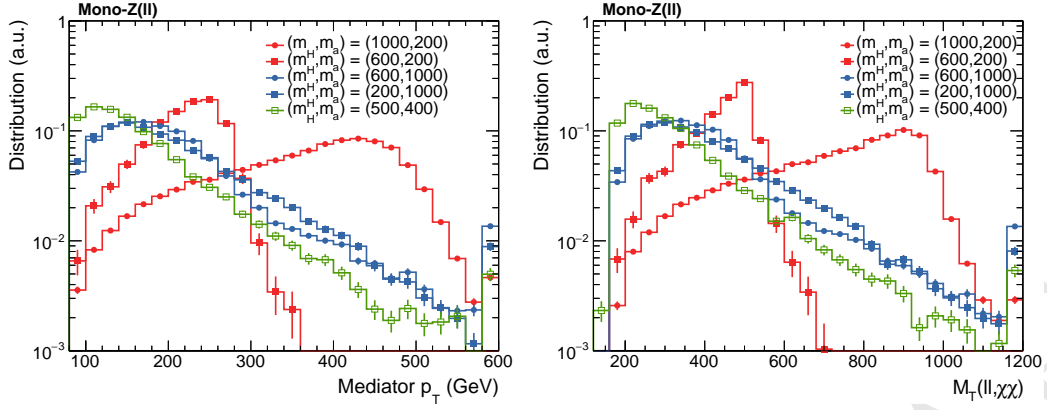


Figure 7: E_T^{miss} and M_T distributions after the full selection of $Z(\text{lep}) + E_T^{\text{miss}}$ search. Both distributions show a peaked structure around M_H in the $M_H > M_a$ regime, reflecting the resonant production of H with a subsequent decay $H \rightarrow aZ$.

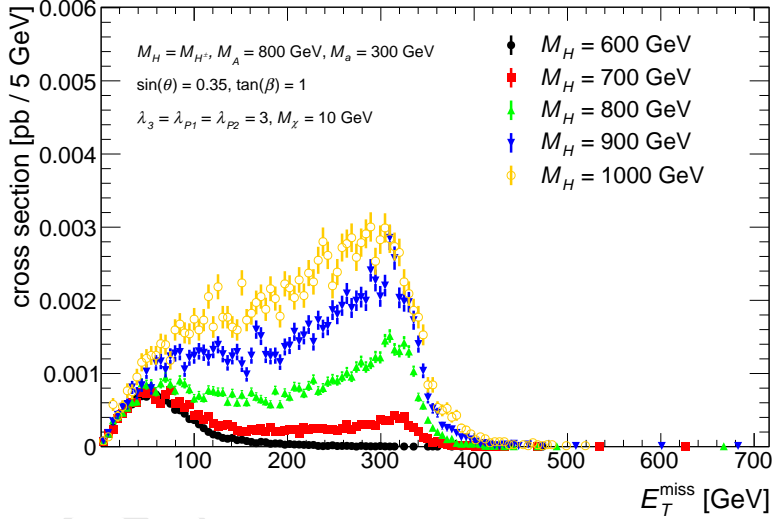


Figure 8: The E_T^{miss} distribution, accounting for the production cross section, of $h(bb) + E_T^{\text{miss}}$ signal events for five representative choices of $M_H = M_{H\pm}$.

Figure 9: E_T^{miss} distribution in $h(bb) + E_T^{\text{miss}}$ and $Z + E_T^{\text{miss}}$ events for different M_H

peaks are quite narrow for values where $\sin \theta$ approaches 1, and $a \rightarrow \chi\bar{\chi}$ is the dominant $\chi\bar{\chi}$ production mode, as shown in Figure 10. However, no significant kinematic dependence on $\sin \theta$ is observed in the E_T^{miss} and top quark p_T as shown in Figure 11 before any analysis cuts are applied.

1.2.3 Ratio of the doublet vacuum expectation values ($\tan \beta$)

For mono- h signals, the shape of the E_T^{miss} distribution also has a non-trivial dependence on $\tan \beta$, as can be seen in Figure 13. As discussed in the sensitivity study later, at small $\tan \beta$, the Yukawa coupling to top quark is large and the signal production mode is domi-

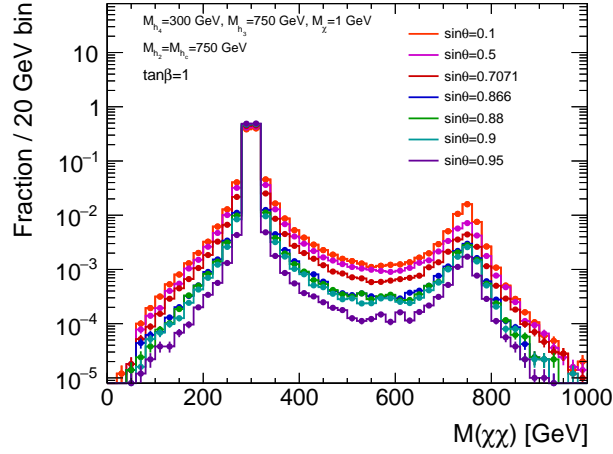


Figure 10: The mass distribution of the $\chi\bar{\chi}$ system for various values of $\sin\theta$, with $M_a = 300$ GeV, $M_A = 750$ GeV, $M_H = M_{H^\pm} = 750$ GeV, and $\tan\beta = 1$.

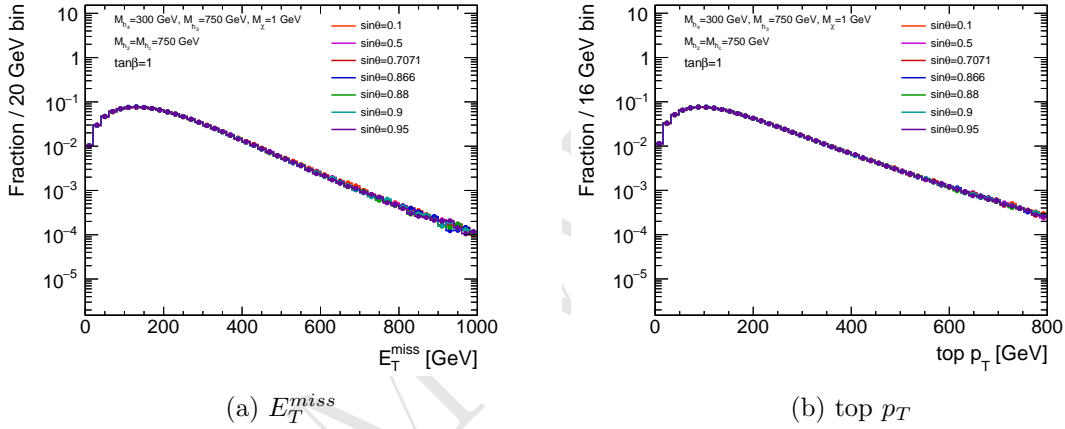
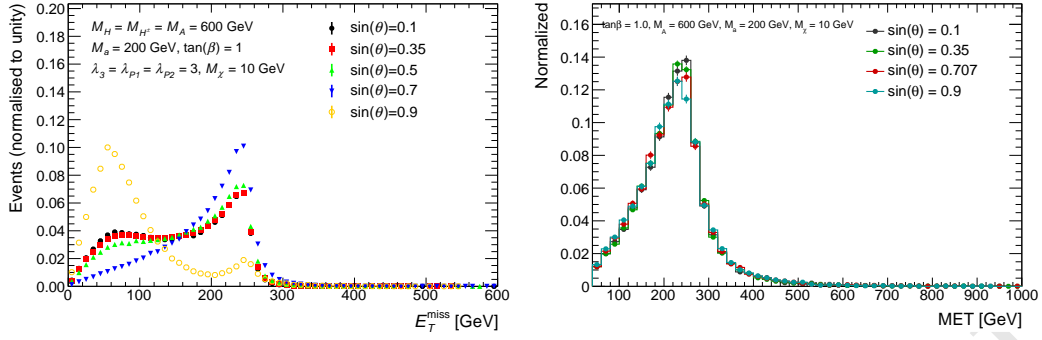


Figure 11: The E_T^{miss} and top p_T distribution for inclusive $t\bar{t} + \chi\bar{\chi}$ production for various values of $\sin\theta$, with $M_a = 300$ GeV, $M_A = 750$ GeV, $M_H = M_{H^\pm} = 750$ GeV, and $\tan\beta = 1$.

nated by the non-resonant 3-body process $gg \rightarrow h\chi\bar{\chi}$, which gives a broad and soft E_T^{miss} spectrum. As $\tan\beta$ increases, Γ_A decreases. With a more narrow A , the relative contribution of resonant A decays increases, and the Jacobian peak grows more pronounced, eventually dominating the E_T^{miss} spectrum. When the on-shell $A \rightarrow a h$ decay is kinematically forbidden, i.e. when $M_A < M_a + M_h$, the shapes of E_T^{miss} distributions become similar and the dependence on $\tan\beta$ almost disappears. For small values of $\tan\beta$ there is a slight softening and broadening of the E_T^{miss} distribution caused by the increased contribution from non-resonant $Z + a$ production in $Z + E_T^{\text{miss}}$ searches.

In the $t\bar{t} + E_T^{\text{miss}}$ signature, and in the limit of small $\tan\beta$ values, the couplings of A (h_3 in the figure) and a (h_4 in the figure) to down-type quarks are heavily suppressed regardless of the Yukawa assignment. At LO, $t\bar{t} + \chi\bar{\chi}$ associated production is mediated



(a) E_T^{miss} distribution for for five representative models with different $\sin \theta$ and fixed scans of $\sin \theta$ for fixed $M_A = M_H = M_{H^\pm} = 600$ GeV, $M_a = 600$ GeV and $M_\chi = 200$ GeV. (b) E_T^{miss} distribution after preselection for fixed $M_A = M_H = M_{H^\pm} = 600$ GeV, $M_a = 600$ GeV and $M_\chi = 200$ GeV.

Figure 12: E_T^{miss} distributions in $h(bb) + E_T^{\text{miss}}$ and $Z(\text{lep}) + E_T^{\text{miss}}$ events for different $\sin \theta$. In both cases, $\tan \beta = 1$ and $M_\chi = 10$ GeV.

through either CP-odd weak eigenstate, A or a , though it is shown in Figure 15 that $a \rightarrow \chi\bar{\chi}$ is the dominant production mode. Although the relative mediator contribution is dependent on $\tan \beta$, observables such as E_T^{miss} and top quark p_T only have a moderate kinematic dependence on $\tan \beta$ as demonstrated in Figure 16 before any analysis cuts. Other variables, such as the transverse mass M_T , are more affected by the contribution of the high mass mediator, as shown in Figure 16 after kinematic cuts.

The production cross-section for a, h, H and A are driven by top-quark loops in the gluon-fusion channel [13], as shown e.g. [as shown in the Feynman diagram], and enhanced for small values of $\tan \beta$. For this reason, and to highlight the complementarity of the $H + E_T^{\text{miss}}$ and $Z + E_T^{\text{miss}}$ signatures, the main focus of the parameter scans should be on the small $\tan \beta$ region. *Setting $\tan \beta$ to unity* leads to a sufficiently large on-shell contribution even at low masses. This in turn increases the number of events at higher E_T^{miss} , so that the $H + E_T^{\text{miss}}$ search can have a comparable sensitivity to the $Z + E_T^{\text{miss}}$ search even though it requires higher E_T^{miss} . Moreover, since the cross-section times branching ratio for the $b\bar{b} + E_T^{\text{miss}}$ signature is enhanced at high values of $\tan \beta$ (see Eq. 3.2 and 3.3 in Ref. [7]) *it is desirable to perform a coarse scan in $\tan \beta$ as well.*

It is interesting to note however that the relative total width for the heavy scalar H becomes unphysically large at high $\tan \beta$ when all scalars have the same mass, due to the very large $H \rightarrow aa$ rate. This can be cured by tuning the mass of the heavy scalar so that the coupling between the heavy scalar and the light pseudoscalar g_{Haa} becomes small for this scan only, therefore suppressing the $H \rightarrow aa$ rate that drives the width. An example of the heavy scalar width as a function of $\tan \beta$, with $M_H = M_A = 600$ GeV, $M_{H^\pm} = 664$ GeV, $\sin \theta = 0.35$, $M_\chi = 10$ GeV and $g_{\text{DM}} = 1$ is shown in Fig. 17.

Even though this choice of parameters for this scan introduces a specific tuning and therefore model-dependence, it can be justified by noting that the trilinear scalar couplings are very sensitive to changes in the model's masses and couplings, and this in turn changes

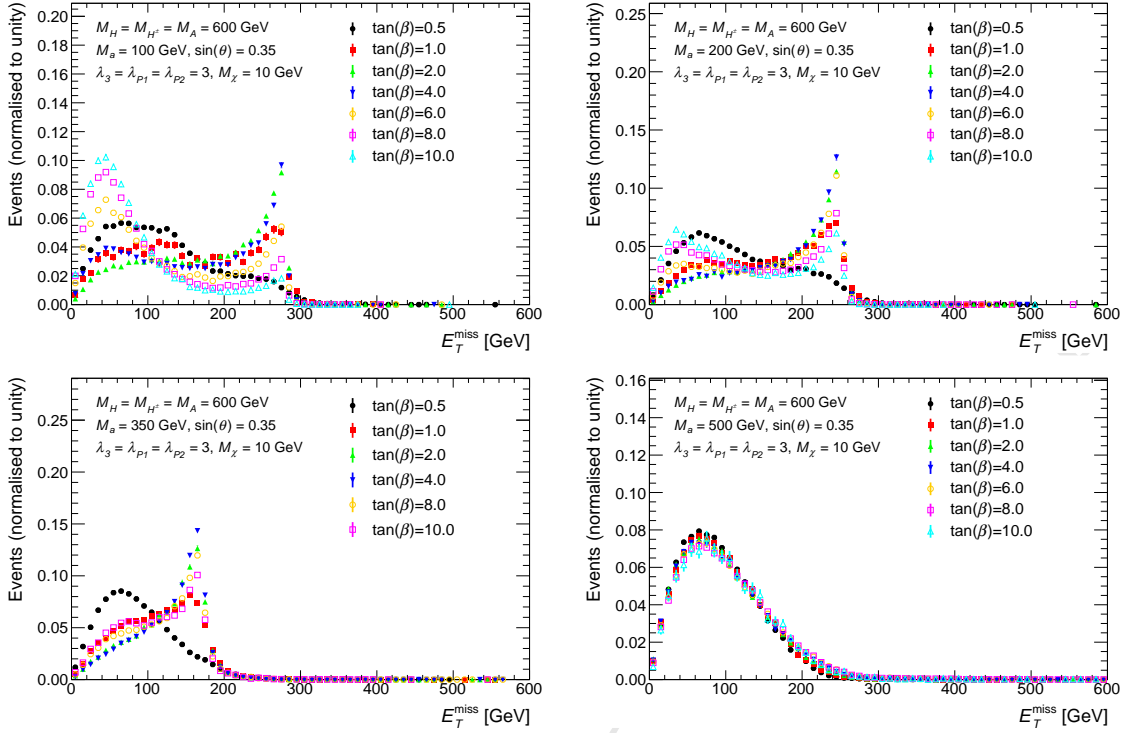


Figure 13: Missing transverse momentum distribution of $h \rightarrow b\bar{b} + E_T^{\text{miss}}$ signal events at parton level with different $\tan\beta$ and fixed $M_A = M_H = M_{H^\pm} = 600$ GeV, $M_\chi = 10$ GeV, $\sin\theta = 0.35$, and $\lambda_{P1} = \lambda_{P2} = \lambda_3 = 3$. The values of M_a are set to 100, 200, 350, and 500 GeV, respectively. The shapes of the E_T^{miss} distributions for different $\tan\beta$ are similar when $M_A < M_h + M_a$. Note, in these figures, both the contributions of gg and $b\bar{b}$ initiated processes are included and a combined histogram is produced according to their corresponding cross sections.

the decay partner of the heavy scalar and of the Higgs partners. Furthermore, the Higgs width does not influence the $b\bar{b} + E_T^{\text{miss}}$ signal directly. Nevertheless, if this is tuning is not performed, particular care has to be taken at high $\tan\beta$ values to obtain reasonable results outside the narrow-width approximation, both for the generation of the signal and for the interpretation of the results.

1.2.4 Mass of DM fermion (M_χ)

The mass of the DM fermion M_χ can change the total cross section and shape of the E_T^{miss} distribution, depending on the mass hierarchy of the A, a, h, χ particles. This is demonstrated in Figure 19. Provided on-shell decays $a \rightarrow \chi\chi$ are possible, i.e., $M_\chi < M_a/2$, the exact value of M_χ has no effect on either kinematics or the total cross section. The only exception is the case $M_a/2 > M_\chi > \frac{1}{2}(M_a - M_h)$. In this M_χ range, the non-resonant process $a \rightarrow hA^*(\chi\chi)$ is kinematically inaccessible. This reduces the overall cross section relative to the $M_\chi \leq \frac{1}{2}(M_a - M_h)$ case, and slightly changes the soft part of the total E_T^{miss} spectrum. However, since the contribution of the $a \rightarrow hA^*(\chi\chi)$ process is minor in any

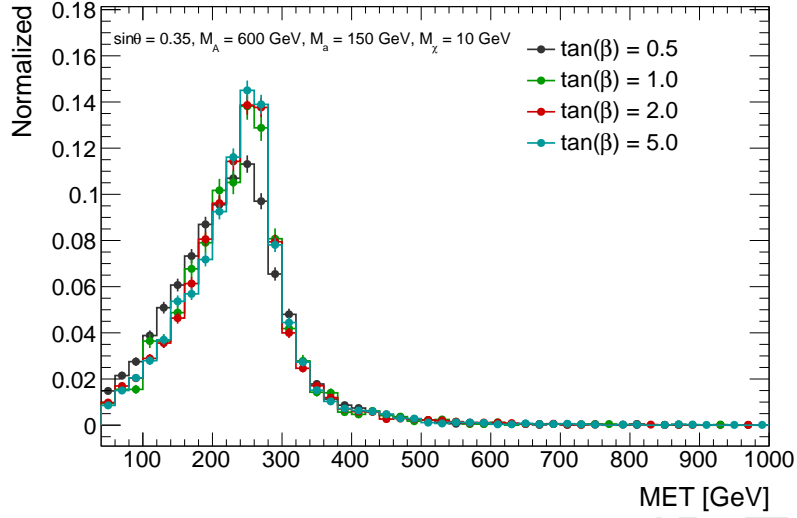


Figure 14: E_T^{miss} distribution after preselection for scans of $\tan\beta$ for fixed $M_A = 600$ GeV and $M_a = 150$ GeV. This parameter has little impact on the kinematic distributions, except for small values of $\tan\beta$ where there is a slight softening and broadening of the E_T^{miss} distribution caused by the increased contribution from the top box feynman diagram.

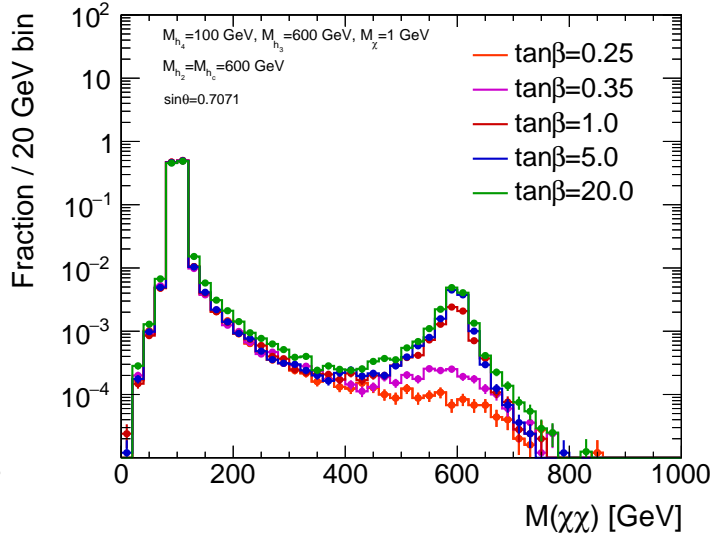


Figure 15: The mass distribution of the $\chi\bar{\chi}$ system for various values of $\tan\beta$, with $M_a = 100$ GeV, $M_A = 600$ GeV, $M_H = M_{H^\pm} = 600$ GeV, and $\sin\theta = 0.7071$.

case, the differences are negligible.

If the DM particle mass is exactly on threshold, i.e., $M_\chi = M_a/2$, the total cross section is resonantly enhanced. This resonant threshold enhancement drops rapidly towards both higher and lower M_χ . Furthermore, the shape of the E_T^{miss} distribution at threshold, where amplitudes involving $a \rightarrow \chi\chi$ decays make up a larger fraction of the signal, differs

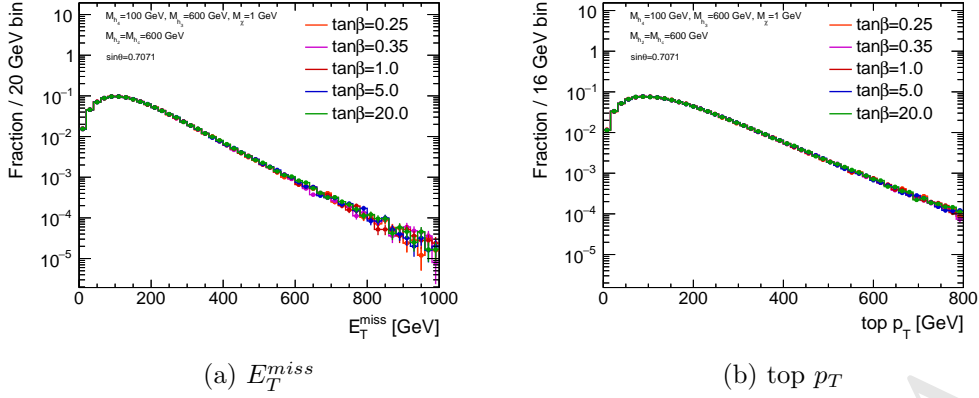


Figure 16: The E_T^{miss} and top p_T distribution for inclusive $t\bar{t} + \chi\bar{\chi}$ production for various values of $\tan\beta$, with $M_a = 100$ GeV, $M_A = 600$ GeV, $M_H = M_{H^\pm} = 600$ GeV, and $\sin\theta = 0.7071$.

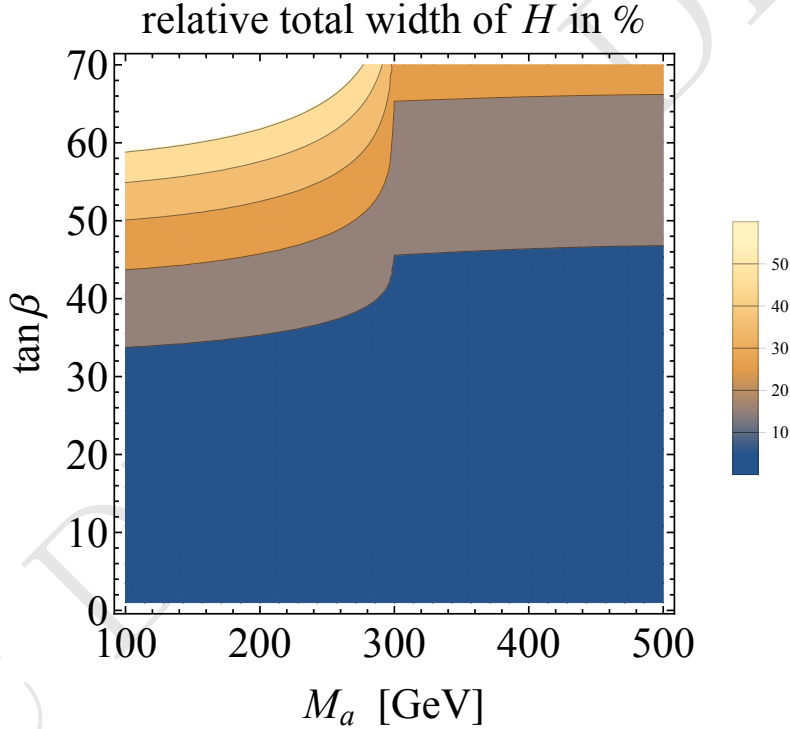


Figure 17: The width of the heavy scalar as a function of $\tan\beta$, with $M_H = M_A = 600$ GeV, $M_{H^\pm} = 664$ GeV, $\sin\theta = 0.35$, $M_\chi = 10$ GeV and $g_{DM} = 1$.

significantly from the one below threshold. Below threshold ($M_\chi > M_a/2$), the total cross section quickly drops by several orders of magnitude. In this regime, the shape of the E_T^{miss} distribution changes with M_χ continuously.

Similar effects are seen in Figure 20. In the $M_\chi < \frac{M_a}{2}$ region, M_χ has no effect on event yield or E_T^{miss} distribution, at $M_\chi = \frac{M_a}{2}$ a resonant enhancement to the cross section

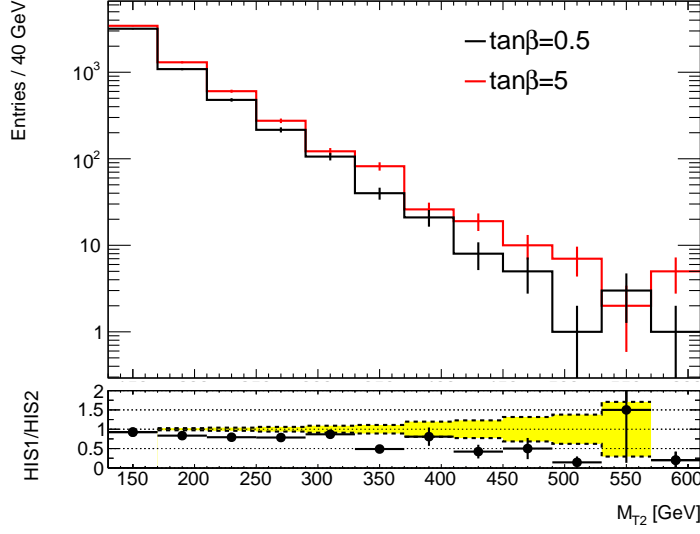


Figure 18: The M_T distribution in the $t\bar{t} + E_T^{\text{miss}}$ signature for different values of $\tan\beta$, after all selection cuts.

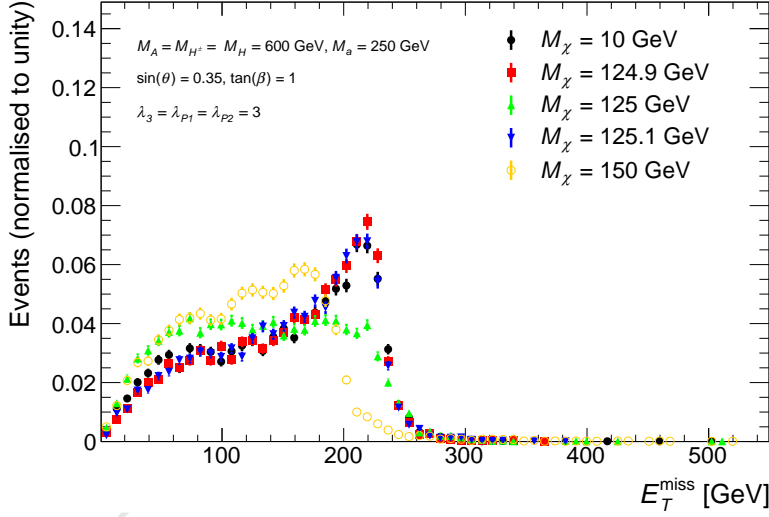


Figure 19: Missing transverse momentum distribution of $h(bb) + E_T^{\text{miss}}$ signal events at parton level for five representative models with different M_χ and fixed $M_A = M_H = M_{H^\pm} = 600$ GeV $M_a = 250$ GeV, $\sin\theta = 0.35$, $\tan\beta = 1$ and $\lambda_{P1} = \lambda_{P2} = \lambda_3 = 3$. The shape of the E_T^{miss} distribution does not change for $M_\chi < M_a/2$, then changes significantly for $M_\chi \geq M_a/2$.

occurs, and in the off-shell region where $M_\chi > \frac{M_a}{2}$ cross section steeply drops. The E_T^{miss} shape remains the same up to, and even slightly above, $M_\chi = \frac{M_a}{2}$, but further off shell the E_T^{miss} distribution becomes increasingly disperse. For $M_\chi = 200$ GeV, DM can still decay on-shell through the A . For $M_\chi = 500$ GeV both pseudoscalars are off-shell leading

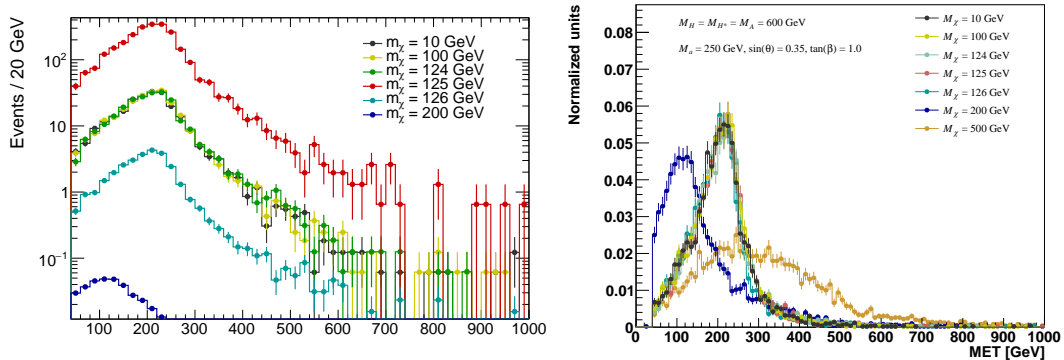


Figure 20: E_T^{miss} distributions following preselection in the $Z(\text{lep}) + E_T^{\text{miss}}$ search are shown (left) scaled to 40 fb^{-1} and (right) normalized to unity for different values of M_χ with fixed $M_A = 600 \text{ GeV}$ and $M_a = 250 \text{ GeV}$.

to an event yield too low to fit on the figure on the left and a E_T^{miss} distribution without structure.

A value of $M_\chi=10$ is chosen as the baseline for the following studies, as it produces a cross-section that is sufficiently large for this model to be detected with Run-2 LHC data and highlights the resonant features of the E_T^{miss} spectrum.

1.3 Comparison with existing pseudoscalar models and recasting of HF+ E_T^{miss} search results

To date, simplified models of DM [14, 15] that add a single scalar or pseudoscalar mediator and the DM particle to the SM are used as benchmarks for the Run II CMS and ATLAS HF+ E_T^{miss} searches. These are called **DMsimp** models in the following. The kinematics and cross-section of the pseudoscalar **DMsimp** models can map directly onto those of the 2HDM+a model, when accounting for the contributions from the light and heavy pseudoscalar mediators.

The comparison of some of the relevant kinematic distributions between the pseudoscalar simplified model and the 2HDM+a model using two different values of M_a , is shown in Figure 21. In these figures, the parameters used are: $M_A = 600 \text{ GeV}$, $M_H = M_{H^\pm} = 600 \text{ GeV}$, $\sin \theta = 0.7071$, $\tan \beta = 1$, while M_a is either 100 or 600 GeV. The distributions for the two models agree when the mediator mass in the **DMsimp** model is set to M_a and the contribution from A decays is smaller since A is more massive than a .

The **DMsimp** model has only one mediator particle. Figure 22 shows that the 2HDM+a model can be represented as the sum of two contributions, one from the light pseudoscalar and the other one from the heavy pseudoscalar. This is because the HF+ E_T^{miss} signatures are dominantly produced in diagrams involving the invisible decays of the two CP-odd scalars. The 2HDM+a model is equivalent to the single pseudoscalar simplified model **DMsimp** when A is much heavier than a , and therefore the former does not contribute to the considered final state. However, when the two mediators are closer in mass, the $pp \rightarrow ttA$ contribution becomes more relevant. This can be seen in Figure 23, where the

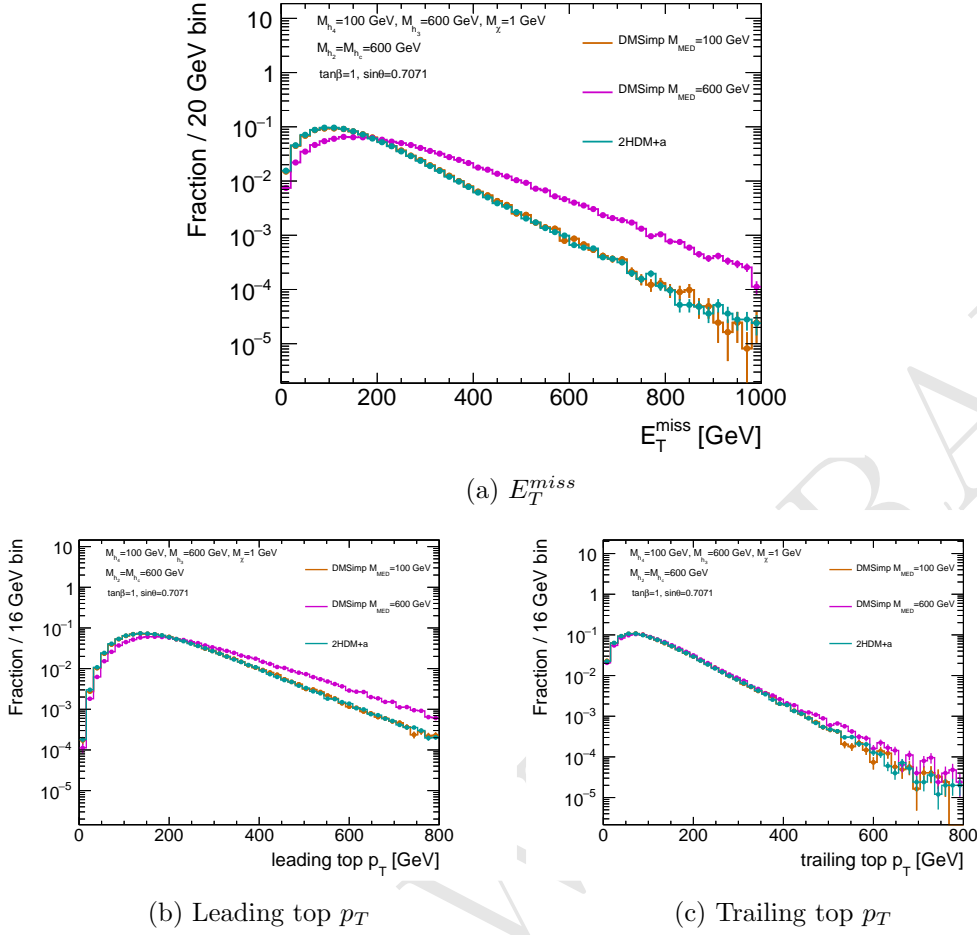


Figure 21: The E_T^{miss} , leading and trailing top p_T distributions for inclusive $t\bar{t} + \chi\bar{\chi}$ production for different values of M_a , with $M_A = M_H = M_{H^\pm} = 600$ GeV, $\tan\beta = 1$, $M_\chi = 1$ GeV and $\sin\theta = 0.7071$, compared to the DMSimp pseudoscalar model.

two models are compared assuming $m(A) = 750$ GeV and two different values for $m(a)$. An excellent agreement is observed between DMSimp and 2HDM+a at parton-level variables sensitive to the helicity structure of the interaction between top and the mediator[16], if the invariant mass of the two DM particles in the 2HDM is smaller than 200(300) GeV for $m(a) = 150(300)$ GeV respectively. This gives confidence that, once the contribution from A production is identified and separated, it is possible to fully map the $2HDM + a$ kinematics to the existing DMSimp model.

The mapping that can be used to reinterpret existing searches that use the DMSimp model is achieved by taking, for each set of the parameters, the average of the selection acceptances for $m(A)$ and $M(A)$ obtained from the DMSimp model, weighted by the respective cross-section for A (σ_A) and a (σ_a) production:

$$Acc_{2HDM}(m(A), M(a)) = \frac{\sigma_a \times Acc_{DMSimp}(m(a)) + \sigma_A \times Acc_{DMSimp}(m(A))}{\sigma_a + \sigma_A} \quad (1.2)$$

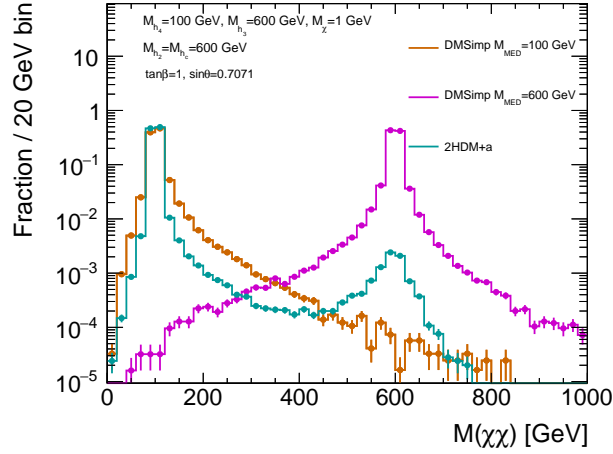


Figure 22: The mass distribution of the $\chi\bar{\chi}$ system for DMSimp pseudoscalar models with $M_a = 100$ GeV and $M_a = 600$ GeV, compared with 2HDM+a with $M_a = 100$ GeV, $M_A = 600$ GeV, $M_H = M_{H^\pm} = 600$ GeV, $\sin\theta = 0.7071$ and $\tan\beta = 1$. TODO: needs different markers.

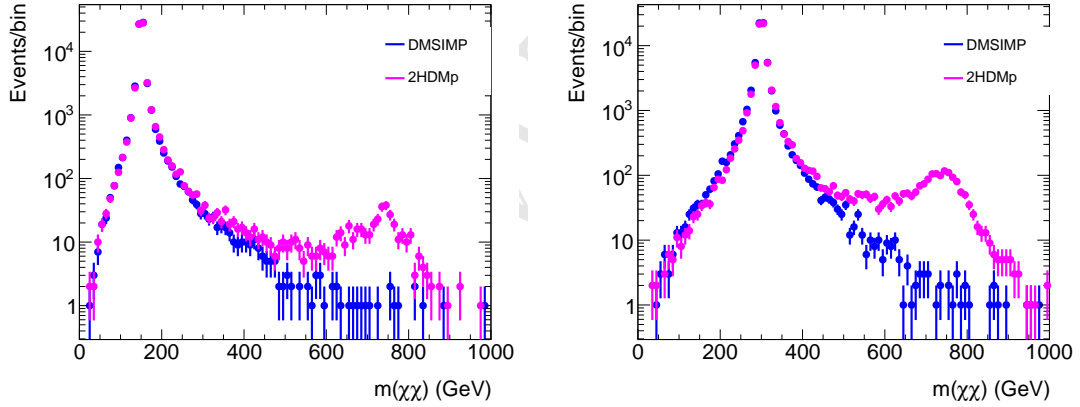


Figure 23: Comparison of $m(\chi\chi)$, the invariant mass of the two DM particles for the DMSimp (blue) and the 2HDMp model (magenta) with $m(A) = M_{med} = 750$ GeV. The plot on the left uses $M_a = 150$ GeV, while the plot on the right uses $M_a = 300$ GeV.

The acceptance in this case is obtained as a parton-level implementation of the two-lepton analysis described in [arXiv:1710.11412]. The acceptance estimated in this way is shown as red triangles in Figure 24, and an excellent agreement can be seen with the acceptances evaluated directly on the 2HDM samples. Further validation was performed also on the acceptances calculated as a function of $\sin\theta$ and $\tan\beta$. Finally, the formula was successfully tested also with $|M_A - M_a| \sim 50$ GeV, where interference between the production of the two bosons is possible.

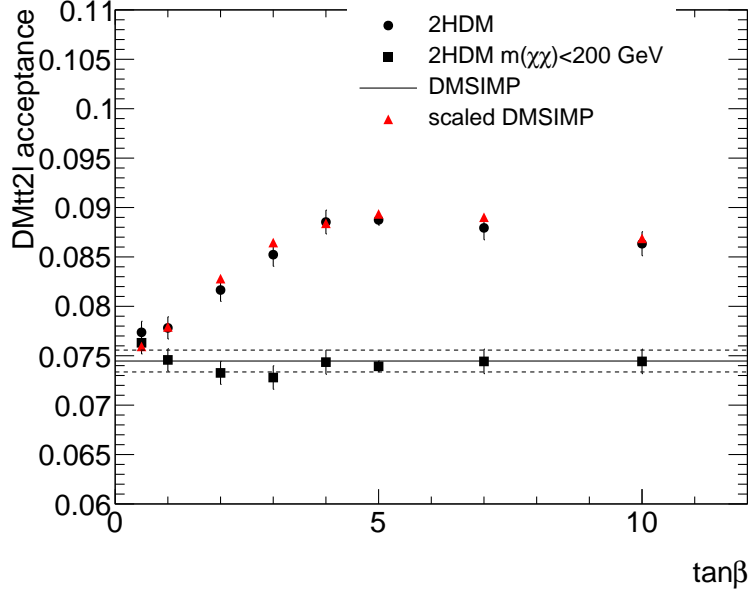


Figure 24: Acceptance of the two-lepton analysis as a function of $\tan\beta$ for the $2HDMp$ model (round markers), for the $2HDMp$ model considering only events with $m(\chi\chi) < 200$ GeV (square markers), and for the $DMSIMP$ model (full line) for a mediator mass of 150 GeV. The two dashed lines indicate the statistical error of the $DMSIMP$. The value of $m(A)$ is fixed at 600 GeV, and $\sin\theta = 0.35$. The acceptance calculated from the $DMSIMP$ acceptance rescaled following the prescription in Equation 1.2 (red triangles) is also shown.

2 Parameter grid

The studies in the previous section show that varying most of the model parameters lead to non-trivial modifications of the for the $H+E_T^{\text{miss}}$ and $Z+E_T^{\text{miss}}$ searches. We decide to investigate the model parameter space through two-dimensional and one-dimensional scans of five parameters: the light pseudoscalar mass (M_a), the heavy pseudoscalar mass (M_A) that we set equal to the mass of the heavy and charged Higgs bosons ($M_A = M_H = M_{H^\pm}$), the mixing angle $\sin\theta$, the ratio of VEVs of the Higgs doublets $\tan\beta$ and the dark matter particle mass M_χ . The benchmark model points that have been agreed within the DMWG and are suggested here do not provide an exhaustive scan the entire parameter space of this model, but highlights many of the features that are unique of this model and showcases the complementarity of the various signatures.

Scan in the $M_a, M_A = M_H = M_{H^\pm}$ plane The main parameter grid proposed to investigate this model with LHC data spans combinations of the light pseudoscalar mass (M_a) and the heavy pseudoscalar mass (M_A) plane, fixing $M_A = M_H = M_{H^\pm}$. The mixing angle $\sin\theta$ is fixed to 0.35 (leading to asymmetric mixing between the pseudoscalars), to evade precision constraints. $\tan\beta$ is fixed to unity to obtain a mixture of resonant and non-resonant processes for the $H+E_T^{\text{miss}}$ and $Z+E_T^{\text{miss}}$ searches. The DM particle mass is

fixed to 10 GeV, to obtain cross-sections that are sufficiently large to be probed by Run-2 LHC searches. The spacing of the grid in M_a and M_A is left to the individual searches. The parameters $\sin\theta$, $\tan\beta$ and M_χ are scanned separately.

Scan in the $M_a, \tan\beta$ plane A two-dimensional scan in the $M_a, \tan\beta$ plane, fixing $M_A = M_H = M_{H^\pm} = 600$ GeV, is used to emphasize the complementarity of the $H+E_T^{\text{miss}}$ and $Z+E_T^{\text{miss}}$ searches with the heavy flavor + E_T^{miss} searches. The scan in M_a includes masses between 10 and 350 GeV, while the $\tan\beta$ scan includes $\tan\beta = 50, 45, 40, 35, 30, 25, 20, 15, 10, 5$, where the high- $\tan\beta$ points are of primary interest for the heavy flavor searches.

Scans in $\sin\theta$ Two one-dimensional scans in $\sin\theta$ are also suggested for further comparison of the $H/Z+E_T^{\text{miss}}$ and $b\bar{b}+E_T^{\text{miss}}$ analyses, as the latter is more sensitive at higher values of $\sin\theta$. In the first scan, resonant processes dominate with $M_A = M_H = M_{H^\pm} = 600$ GeV and $M_a = 200$ GeV, while in the second scan $M_A = M_H = M_{H^\pm} = 1000$ GeV and $M_a = 350$ GeV. For both scans, $\tan\beta$ and the DM mass are fixed to $\tan\beta=1$ and $M_\chi = 10$ GeV. [TODO: add statement about precision constraints?]

Scan in M_χ A one-dimensional scan in M_χ spanning from 1 GeV to 500 GeV, with fixed $M_A = M_H = 600$ and $M_a = 250$ GeV, is also suggested to connect this model to a standard cosmological history. Even though the model points with where the DM particle has a mass above 100 GeV are not within immediate reach of Run-2 searches, the measured relic density is satisfied by this model at values of DM mass around 100 GeV, as shown in [section 5](#).

3 Sensitivity studies

In the first part of this section we present the sensitivity estimates for two of the main signatures that are sensitive to the model, the Higgs+ E_T^{miss} and the $Z+E_T^{\text{miss}}$ signatures, in the parameter scans chosen for comparison. These estimates are based on generator-level reinterpretation of existing results with 36 fb^{-1} of LHC data at a center-of-mass energy of 13 TeV. These results contain different amounts of public information. In the case of the Higgs+ E_T^{miss} from [5], model-independent limits are used for the reinterpretation, while for the $Z+E_T^{\text{miss}}$ signature an estimate of the sensitivity is obtained using generator-level information from signal and background simulations.

The second part of this section briefly outlines additional signatures that are also sensitive to this model. Firstly we briefly discuss the jet + E_T^{miss} signatures and the heavy flavor + E_T^{miss} signatures, which do not yet have sensitivity with the 36 fb^{-1} dataset for most of the scans. Then we enumerate other signatures that can be sensitive to this model, emphasizing those that are not yet fully covered by experimental searches.

3.1 Studies of the $h(bb) + E_T^{\text{miss}}$ signature

The sensitivity estimates of the ATLAS and CMS $h(bb) + E_T^{\text{miss}}$ searches to the 2HDM+a scenarios are based on limits on the minimally model-dependent anomalous production of 125 GeV Higgs bosons in association with E_T^{miss} in [5]. As these limits are set in terms

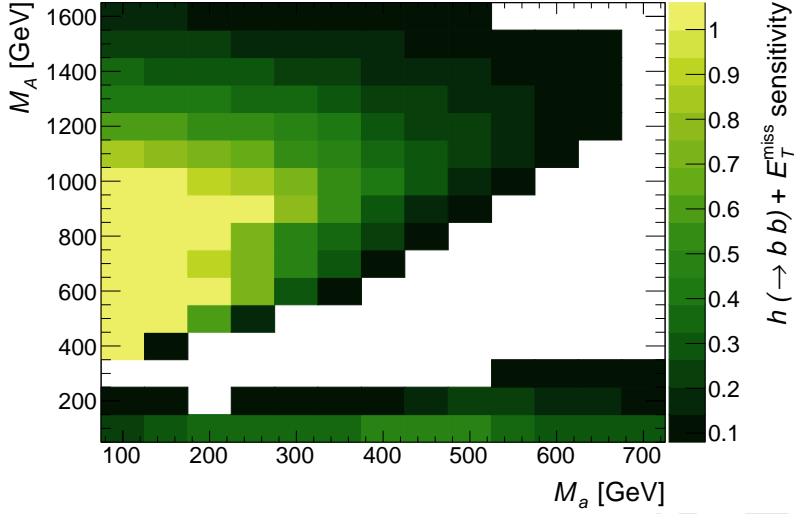


Figure 25: Sum over all E_T^{miss} -bins of the estimated sensitivity to $H \rightarrow b\bar{b} + E_T^{\text{miss}}$ events as a function of (M_A, M_a) . The sensitivity, defined as the sum of Equation 3.1 over the E_T^{miss} bins, is based on the limits with reduced model dependence from Ref. [5]. The remaining parameters take the values $M_H = M_{H^\pm} = M_A$, $\sin \theta = 0.35$, $\tan \beta = 1$, $M_\chi = 10$ GeV and $\lambda_{P1} = \lambda_{P2} = \lambda_3 = 3$. Bins with no content have a negligible sensitivity.

of the observed production cross-section of non-SM events with large E_T^{miss} and a Higgs boson, they can be compared directly to the cross-sections obtained from the 2HDM+a model after folding the detection efficiency ε times the kinematic acceptance \mathcal{A} of the event selection. This approach reduces the need for computing resources to simulate further event generation steps and detector response. The variable of interest for the sensitivity study of the $h(bb) + E_T^{\text{miss}}$ searches is the ratio between the parton-level cross-section $\sigma_i^{\text{parton}, h+\text{DM}}$ times the $H \rightarrow b\bar{b}$ branching ratio $\mathcal{B}^{\text{SM}, h \rightarrow b\bar{b}}$ predicted by the SM for the 125 GeV Higgs boson, multiplied by the acceptance \mathcal{A} and detector efficiency ε , and the upper observed cross-section of the anomalous production of Higgs bosons in association with E_T^{miss} ($\sigma_i^{\text{obs}, h(bb)+E_T^{\text{miss}}}$):

$$\mathcal{S}_i \equiv \frac{\sigma_i^{\text{parton}, h+\text{DM}} \times \mathcal{B}^{\text{SM}, h \rightarrow b\bar{b}} \times (\mathcal{A} \times \varepsilon)_i}{\sigma_i^{\text{obs}, h(bb)+E_T^{\text{miss}}}}, \quad (3.1)$$

where is the $H \rightarrow b\bar{b}$ branching ratio predicted by the SM for the 125 GeV Higgs boson. This quantity is summed over the i E_T^{miss} bins of the search, since the model will populate more than one E_T^{miss} bin at a time. A particular point in the space is excluded by the current search if $\mathcal{S}_i \geq 1$.

The expected sensitivity of $h(bb) + E_T^{\text{miss}}$ searches to the 2HDM+a model in the (M_a, M_A) plane is shown in Figure 25. The sensitivity decreases with increasing $M_A = M_H = M_{H^\pm}$ for $M_A \geq 1$ TeV because the fraction of resonant signal events drops. This drop is caused by increasingly large Γ_A , which allows for an increasing fraction of non-resonant signal events, driven by events with very off-shell A . Near the mass diagonal

$M_a = M_A$, there is little to no sensitivity. This is because the Jacobian peak moves to low E_T^{miss} for a small mass splitting $|M_A - M_a|$ (as shown in Equation 1.1, Figure 1a, and Figure 1b). Moreover, the coupling g_{Aah} is small when all Higgs bosons are nearly degenerate in mass, cf. Equation 4.12 in Ref. [7], resulting in a small total cross section and therefore a further decrease in sensitivity. The sensitivity above the mass diagonal, $M_A > M_a$, is larger than below the mass diagonal. Two parameter choices cause this asymmetry:

1. The choice of $M_A = M_H = M_{H^\pm}$ forces the neutral and charged CP -even scalars to have lower masses below the diagonal and higher masses above the diagonal, leading to configurations with a lower fraction of resonant signal events. One can use Figure 8 to exemplify this behaviour. Considering the symmetry between the two pseudoscalars, when the neutral and charged scalars $M_H = M_{H^\pm}$ are lighter than one of the two pseudoscalars (marked as A in the figure, but effectively representing a in the case of this scan because of the symmetry), one can see that non-resonant configurations are preferred. This also yields a reduced total cross-section.
2. The choice of $\sin \theta = 0.35 \neq 1/\sqrt{2}$ means that the mixing between the pseudoscalars A and a is asymmetric. A couples more strongly to SM particles than a , while the opposite happens to the DM fermion χ . The situation below the diagonal corresponds to the case of $\sin \theta = \sqrt{1 - 0.35^2} \approx 0.938$ and $M_A > M_a$. As it can be seen in Figure 12a, this $\sin \theta$ configuration yields a higher fraction of non-resonant signal events with low E_T^{miss} , and correspondingly a lower sensitivity is found, as also seen in Figure 27.

The scan of the sensitivity in the $(M_a, \tan \beta)$ plane is shown in Figure 26. At very low $\tan \beta$, the Yukawa coupling to top quarks is large, and most of the signal events come from non-resonant processes, as can be seen from Figure 13. The non-resonant processes are characterised by soft E_T^{miss} , which lowers the kinematic acceptance and reduces the sensitivity of the search. For higher $\tan \beta$, the fraction of resonant events increases due to the reduced top Yukawa coupling, resulting in an increase of sensitivity. However, reducing the top Yukawa coupling also reduces the total production cross section. Above $\tan \beta \approx 1.2$, the sensitivity loss due to reduced cross section outpaces the sensitivity gain due the resonant signal. At very high $\tan \beta$ (≥ 10), this trend is reversed again because the $\tan \beta$ enhancement² of the coupling to b -quarks compensates for the small b -quark mass. At this point bb initiated processes start to dominate the production cross section and drive the increase in sensitivity.

The sensitivity as a function of $\sin \theta$ is shown in Figure 27. The sensitivity vanishes at $\sin \theta = 0$ and $\sin \theta = 1$, since those values correspond to no mixing between A and a , and thus no connection between the SM and the dark sector. For its intermediate values, the $\sin \theta$ parameter influences the couplings of the pseudoscalars to DM as well as to SM fermions, as well as the coupling strength of the trilinear scalar vertices such as g_{Aah} [7]. Increasing these couplings increases the total cross section, but it can also increase Γ_A and

²The 2HDM+a scenario assumes a Yukawa sector of type II.

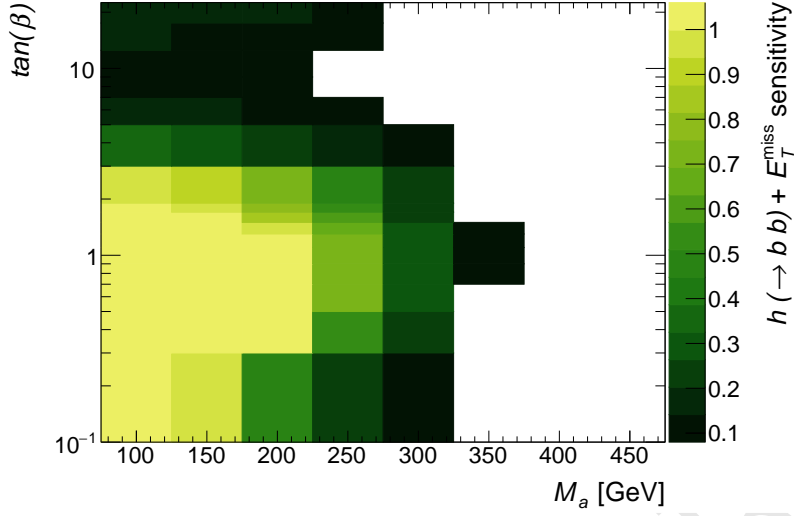


Figure 26: Sum over all E_T^{miss} -bins of the estimated signal sensitivity to $h \rightarrow bb + E_T^{\text{miss}}$ events as a function of $(M_a, \tan \beta)$. The sensitivity, defined as the sum of Equation 3.1 over the E_T^{miss} bins, is based on the limits with reduced model dependence from Ref. [5]. The remaining parameters take the values $M_H = M_{H^\pm} = M_A = 600$ GeV, $\sin \theta = 0.35$, $M_\chi = 10$ GeV and $\lambda_{P1} = \lambda_{P2} = \lambda_3 = 3$. Bins with no content have a negligible sensitivity.

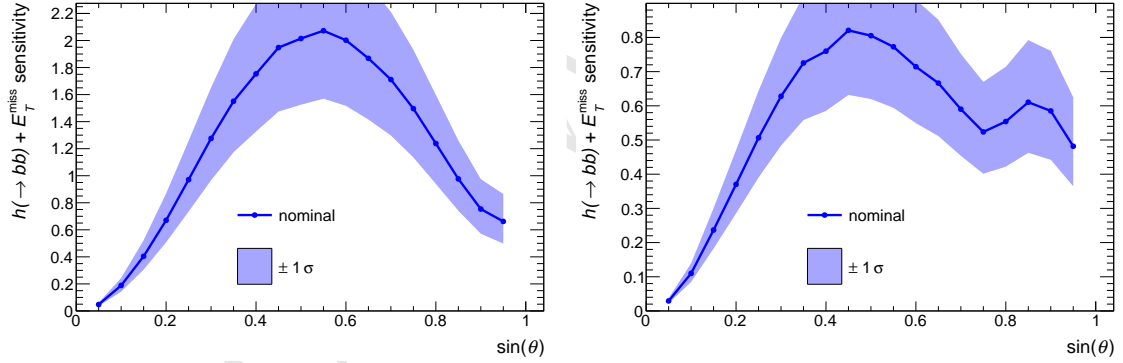


Figure 27: Sum over all E_T^{miss} -bins of the estimated signal sensitivity to $h \rightarrow bb + E_T^{\text{miss}}$ events as a function of the pseudoscalar mixing parameter $\sin \theta$, for $M_a = 200$ GeV and $M_H = M_{H^\pm} = M_A = 600$ GeV (left) as well as $M_a = 350$ GeV and $M_H = M_{H^\pm} = M_A = 1000$ GeV (right). The remaining parameters take the values $M_\chi = 10$ GeV, $\tan \beta = 1$, and $\lambda_{P1} = \lambda_{P2} = \lambda_3 = 3$. The sensitivity, defined as the sum of Equation 3.1 over the E_T^{miss} bins, as well as the uncertainty on the sensitivity (shaded blue) are based on the limits with reduced model dependence from Ref. [5] and the uncertainties described therein. Bins with no content have a negligible sensitivity.

thereby decrease the resonant fraction of signal events and the overall search sensitivity. For this reason, the dependence of the sensitivity on $\sin \theta$ depends on the interplay of the couplings. As a consequence, the sensitivity curve as a function of $\sin \theta$ has more than one

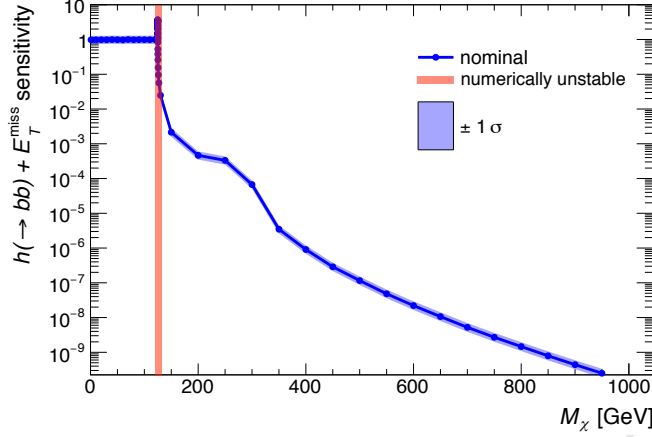


Figure 28: Sum over all E_T^{miss} -bins of the estimated signal sensitivity to $h \rightarrow bb + E_T^{\text{miss}}$ events as a function of the DM mass M_χ . The sensitivity, defined as the sum of Equation 3.1 over the E_T^{miss} bins, as well as the uncertainty on the sensitivity (shaded blue) are based on the limits with reduced model dependence from Ref. [5] and the uncertainties described therein. The remaining parameters take the values $M_a = 250$ GeV, $M_H = M_{H^\pm} = M_A = 600$ GeV, $\sin \theta = 0.35$, $\tan \beta = 1$, and $\lambda_{P1} = \lambda_{P2} = \lambda_3 = 3$. The sensitivity is constant below $M_\chi < M_a/2$, and rapidly drops for $M_\chi > M_a/2$. The sensitivity is resonantly enhanced for $M_\chi = M_a/2$.

local maximum, as shown the right panel of Figure 27.

The sensitivity to models with varying M_χ is shown in Figure 28. Below the threshold of $M_\chi < M_a/2$, the sensitivity is constant since the E_T^{miss} distribution and the total signal cross section remain unchanged. The region at threshold $M_\chi = M_a/2 \pm 5 \text{ GeV}$ (shaded in red in Figure 28) is numerically unstable and should be avoided. Above threshold, the sensitivity drops rapidly because $M_\chi > M_a/2$ requires an off-shell $a^* \rightarrow \chi\chi$ decay, which is strongly suppressed by the typically narrow width of a . The width of a is substantially reduced once $a \rightarrow \chi\chi$ is kinematically inaccessible, as $\Gamma_{a \rightarrow \chi\chi}$ is a large contribution to the total width of a for $M_\chi \leq M_a/2$ [7]. There is a slight increase in sensitivity for $M_\chi \approx M_A/2$ when the $A \rightarrow \chi\chi$ decay hits its kinematic threshold, yet the absolute sensitivity remains negligible.

3.2 Studies of the $Z + E_T^{\text{miss}}$ signature

In the absence of generic limits on anomalous production of $Z + E_T^{\text{miss}}$ events, the expected sensitivity of the $Z + E_T^{\text{miss}}$ searches to this model is approximated comparing the number of generator-level signal events to the respective background estimates.

For the leptonic channel, the published background estimates corresponding to 36 fb^{-1} of 13 TeV data [11] are used, and a reconstruction efficiency of 75% is assumed for signal events. The same selection cuts applied to data in [11] are applied to signal. Signal and

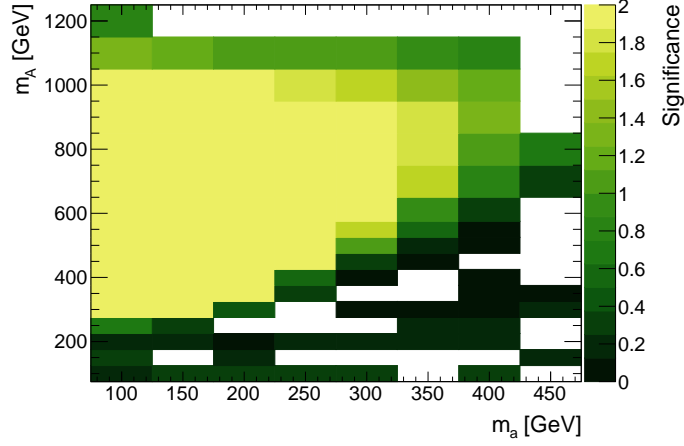


Figure 29: Expected significances for the $Z+E_T^{\text{miss}}$ leptonic signature in the (M_a, M_A) plane. Bins with no content have a negligible sensitivity.

background are binned in the same published E_T^{miss} bins, and a conservative background systematic uncertainty of 20% is assumed for $E_T^{\text{miss}} < 120$ GeV and 10% for $E_T^{\text{miss}} > 120$ GeV.

For the hadronic channel, $Z \rightarrow \nu\nu$ events in association with jets are simulated using Sherpa 2.2.1 [17] and the matrix elements are calculated up to 2 partons at next-to-leading order and up to 4 partons at leading order. Signal and background are scaled to 40 fb^{-1} of 13 TeV data. The $Z(\rightarrow \nu\nu)+\text{jets}$ events are analyzed at particle level with the same criteria used for the signal. The number of $Z \rightarrow \nu\nu$ events after applying the cuts is increased by a factor 2 to conservatively account for the contribution from other backgrounds. This factor is based on the ATLAS dark matter search in the mono- Z hadronic signature using 3.2 fb^{-1} of 13 TeV data ??.

Following the Asimov approximation, the significance for individual bins is calculated as a Poisson ratio of likelihoods modified to incorporate systematic uncertainties on the background [18]:

$$Z'_{bin} = \sqrt{2 \cdot \left((s+b) \ln \left[\frac{(s+b)(b+\sigma_b^2)}{b^2 + (s+b)\sigma_b^2} \right] - \frac{b^2}{\sigma_b^2} \ln \left[1 + \frac{\sigma_b^2 s}{b(b+\sigma_b^2)} \right] \right)} \quad (3.2)$$

This metric has the advantage that it accounts for background systematics and is still valid for $s \gg b$. Similarly to the $h(bb) + E_T^{\text{miss}}$ case, the total significance is defined as the per bin significances summed in quadrature. The ATLAS and CMS experiments are expected to be sensitive to regions with significances greater than 2.

The expected sensitivity of $Z+E_T^{\text{miss}}$ searches to the 2HDM+a model in the (M_a, M_A) plane is shown in Figure 31 for the leptonic case, and Figure 32 for the hadronic case.

The sensitivity for the $Z+E_T^{\text{miss}}$ signatures in the $(M_a, \tan \beta)$ plane is shown in Figure 31

The leptonic $Z+E_T^{\text{miss}}$ search provides experimental coverage of this model for a broad part of the parameter space. The pseudoscalar mediator a can be probed up to mass values

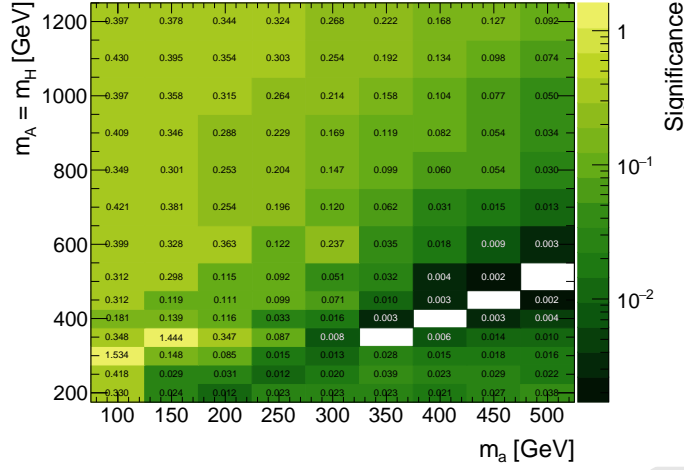


Figure 30: Expected significances for the $Z+E_T^{\text{miss}}$ hadronic signature in the (M_a, M_A) plane, combining both boosted and resolved analyses. Bins with no content have a negligible sensitivity.

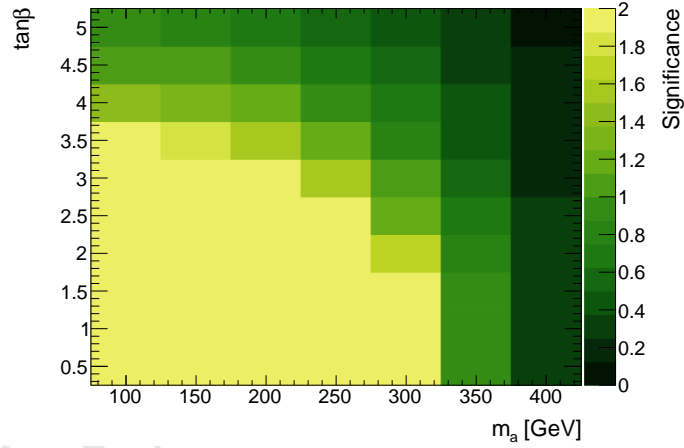


Figure 31: Expected significances for the $Z+E_T^{\text{miss}}$ leptonic signature in the $(M_a, \tan \beta)$ plane. Bins with no content have a negligible sensitivity.

of ≈ 350 GeV, depending on the choice of parameters. Leptonic $Z+E_T^{\text{miss}}$ searches are mostly sensitive in the region of $\tan \beta < 4$. The hadronic $Z+E_T^{\text{miss}}$ search covers a smaller parameter space with respect to the leptonic search, but it is nevertheless complementary.

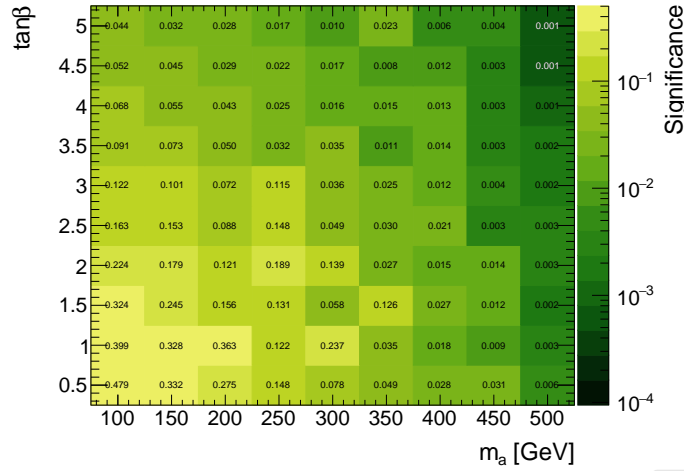


Figure 32: Expected significances for the $Z + E_T^{\text{miss}}$ hadronic signature in the $(M_a, \tan \beta)$ plane, combining both boosted and resolved analyses. Bins with no content have a negligible sensitivity.

3.3 Sensitivity of other signatures

3.3.1 Heavy flavor + E_T^{miss} signatures

The choice of $\sin \theta = 0.35$ and $\tan \beta = 1$ means that the searches with heavy flavors are not sensitive to parameter scans other than the $\tan \beta$ and $\sin \theta$ scans. As discussed in [subsection 1.3](#), it is possible to recast the results of searches reinterpreted with the pseudoscalar model from [14], but this has not been done for this whitepaper.

3.3.2 Jet + E_T^{miss} signature

The search for events with at least one jet and large missing transverse momentum in the final states can be also interpreted in the context of the 2HDM+a model. In this scenario the pseudoscalar mediator can be radiated from heavy quark loops providing such a signature. This channel is able to probe a phase space with low $\tan \beta$ and high $\sin \theta$ in which the cross-sections of this kind of processes are enhanced, as shown in Fig. 13 of [7]. The choice of $\tan \beta = 1$ for the studies in this whitepaper highlights the complementarity between $H + E_T^{\text{miss}}$ and $Z + E_T^{\text{miss}}$ signatures; however the jet + E_T^{miss} signature is only sensitive to values of $\tan(\beta)$ up to 0.5 and is not studied in detail in this whitepaper.

Since the models used for the interpretation of the jet + E_T^{miss} search in terms of scalar DM mediators are the same used for the HF + E_T^{miss} searches, it is possible to reinterpret the results of the search in terms of this model using the same rescaling strategy discussed in [subsection 1.3](#).

4 Phenomenological studies of other signatures of 2HDM+a

This section includes a series of preliminary studies for signatures that have not yet been used for the interpretation of 2HDM+a or other dark matter models. The purpose of

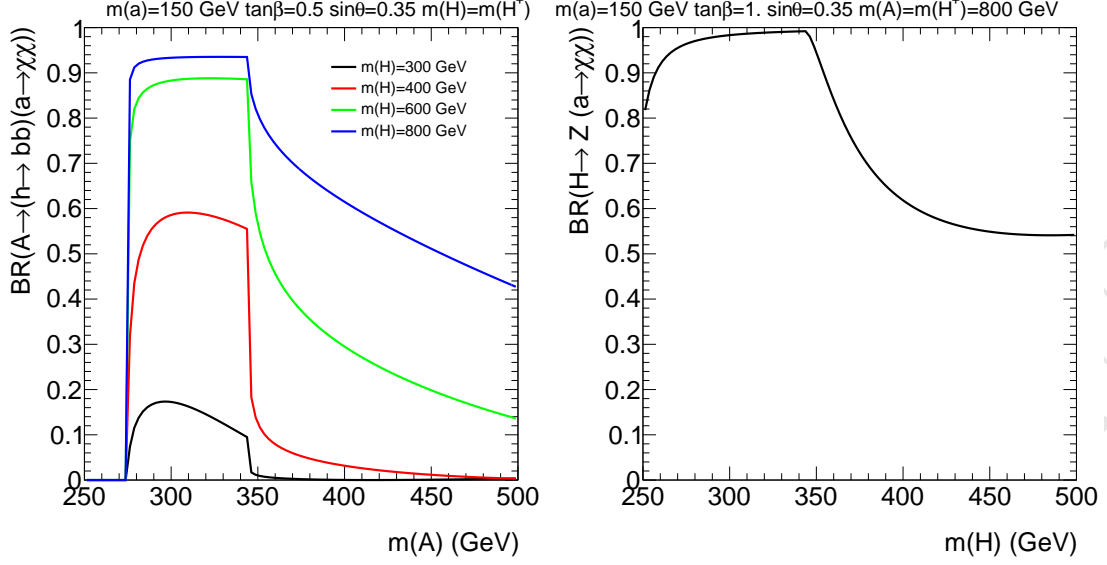


Figure 33: Example of the dependence of the A and H branching ratio into ah as a function of some parameters of the 2HDM model.

this section is to lay the basis for further exploration of this model in these experimental searches.

4.0.1 Signatures with $t\bar{t}h + E_T^{\text{miss}}$

As discussed in subsection 1.3, the production of the heavy mediator A contributes sizably to the $t\bar{t} + E_T^{\text{miss}}$ production cross section in the $2HDM + a$ model. This is also true for the heavy H . When the decay of these mediators into the lightest pseudoscalar a is allowed, this decay process dominates over the direct decay into $\chi\chi$. In analogy with what happens for the mono- h signature discussed in [7], for certain region of parameter space the contribution of the processes $pp \rightarrow t\bar{t}A \rightarrow t\bar{t}ah$ and $pp \rightarrow t\bar{t}H \rightarrow t\bar{t}aZ$ become sizable. In the case of $pp \rightarrow t\bar{t}A \rightarrow t\bar{t}ah$, it can be inferred from Fig. 12(b) of Ref. [7] that for relatively small $m(A)$ the $pp \rightarrow t\bar{t}ah$ cross section can be up to 30% that of the $pp \rightarrow t\bar{t}\chi\chi$ process.

This encourages the study of the interplay of $t\bar{t}h + E_T^{\text{miss}}$ searches with the traditional heavy flavor + E_T^{miss} searches, to understand the complementarity in sensitivity for the two kinds of searches in the various benchmark scenarios. A first step towards such a study is the branching ratio of the 2HDM+ a into A and H (decaying in turn to $t\bar{t}$), shown in Figure 33, showing a sizable contribution.

4.0.2 $tW + E_T^{\text{miss}}$ signature

The sensitivity of the LHC experiments to the associated production of dark matter with a single top has been recently studied [19] in the framework of an extension of the standard model featuring two Higgs doublets and an additional pseudoscalar mediator. This study extends the work of previous literature [20], which demonstrated using a simplified model

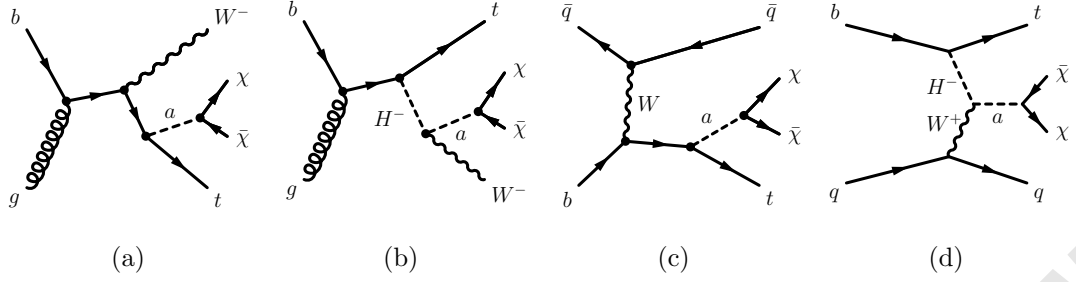


Figure 34: Representative diagrams for tW and t -channel production of DM in association with a single top quark.

that considering final states involving a single top quark and DM (DMt) increases the coverage of existing analyses targeting DM particles produced in association with $t\bar{t}$.

Like single top production within the SM, the DMt signature in the model includes three different types of contributions at leading order (LO) in QCD: t -channel production, s -channel production and associated production together with a W boson (tW) (Fig. 34). When the decay $H^\pm \rightarrow W^\pm a$ is possible, the H^\pm is produced on-shell, and the cross-section of $pp \rightarrow tW\chi\bar{\chi}$, assuming H^\pm masses of a few hundred GeV, is around one order of magnitude larger than the one for the same process in the simplified model. Moreover the production and cascade decay of a resonance yields kinematic signatures which can be exploited to separate the signal from the SM background.

Ref. [19] analyzes detector-smeared generator-level signal and background samples using dedicated selections considering one and two lepton final states, in order to assess the coverage in parameter space for this signature at a centre-of-mass energy of 14 TeV assuming an integrated luminosity of 300 fb^{-1} . Figure 35 shows the reach of this signature for two of the parameter scans proposed in this whitepaper, in the $(M_a, \tan\beta)$ plane assuming $\sin\theta = 0.35$ and $m(A) = m(H^\pm) = m(H) = 500 \text{ GeV}$, and as a function of $\tan\beta$ assuming $\sin\theta = 0.35$, $m(a) = 150 \text{ GeV}$ and $m(A) = m(H^\pm) = m(H) = 500 \text{ GeV}$. The sensitivity of this signature is comparable to the one of the Higgs + E_T^{miss} signature [7].

4.0.3 $t\bar{t}$ resonances

Heavy (pseudo)scalar bosons with $M_{A/H} \geq 2M_t$ and $\tan\beta \sim \mathcal{O}(1)$ will decay dominantly into top-quark pairs. Searches for features in the $t\bar{t}$ invariant mass spectra are sensitive to this process. In this case, interference effects between the signal processes and the SM $t\bar{t}$ production distort the signal shape from a single peak to a peak-dip structure [21].

The results of the first LHC search accounting for this feature in Ref. [22] can be reinterpreted in the context of the 2HDM+a, after modifying the MADGRAPH 5 model to feature this effect. Since interference between loop-induced and tree-level processes cannot currently be simulated, "Higgs_Effective_Couplings_FormFactor" approach from Ref. [22] is adopted, replacing the loop production by an effective vertex. Using this approach, it can be verified that the 2HDM+a reduces to a minimal 2HDM when the pseudoscalar mediator

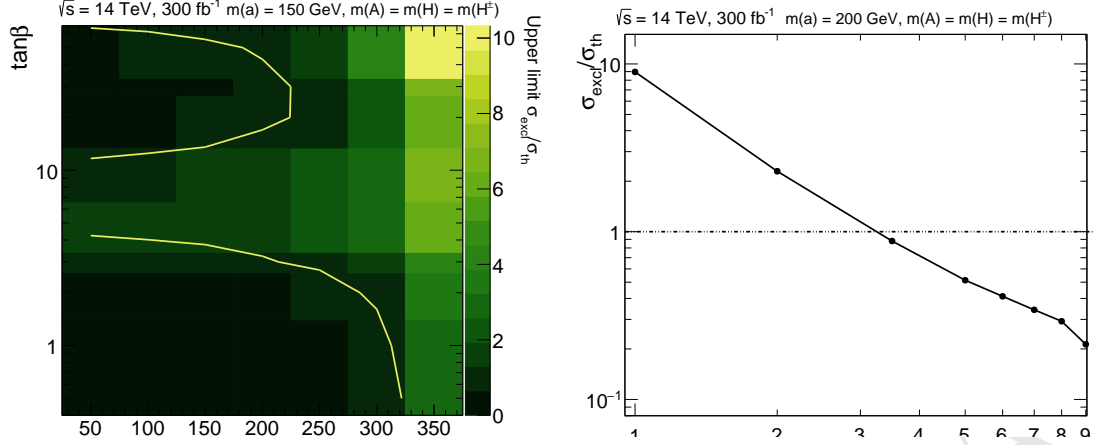


Figure 35: Sensitivity in terms of excluded/theoretical cross-section for the $tW+E_T^{\text{miss}}$ signature in the $(m(a), \tan\beta)$ plane, fixing $m(a)$ to 150 GeV, $\sin\theta = 0.35$ and $m(A) = m(H^\pm) = m(H)$ (left). Sensitivity as a function of $\tan\beta$, assuming $\sin\theta = 0.35$, $m(a) = 150$ GeV and $m(A) = m(H^\pm) = m(H) = 500$ GeV (right).

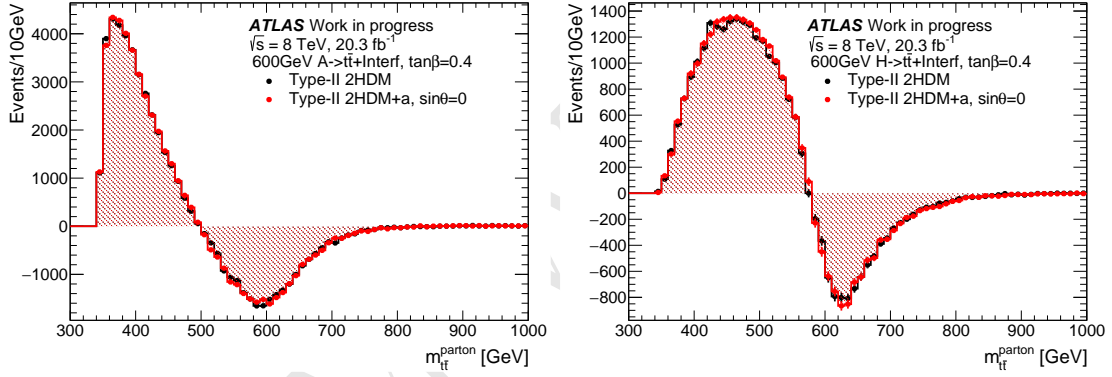
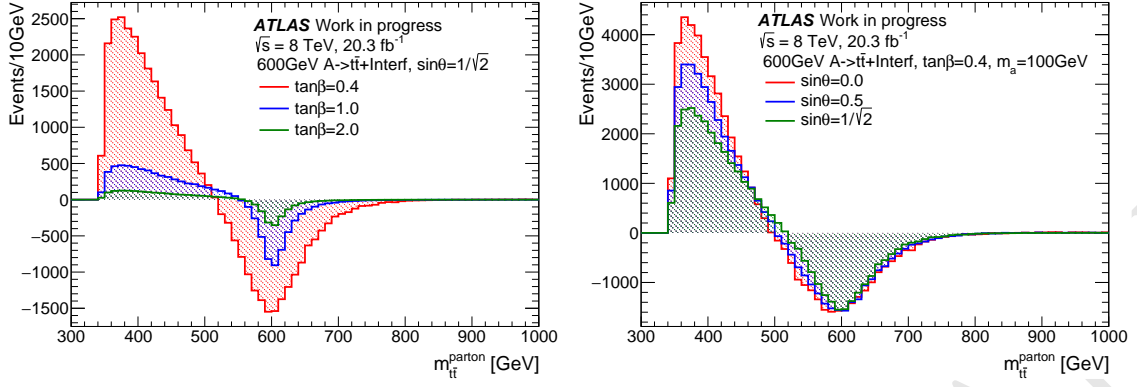


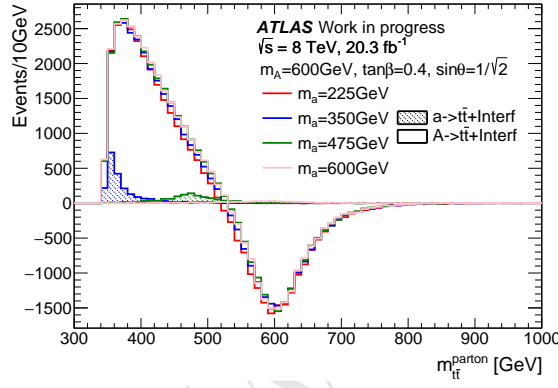
Figure 36: $M_{t\bar{t}}$ distribution of the heavy (pseudo)scalar boson decaying into $t\bar{t}$ with $M_A = M_H = 600\text{GeV}$, $\tan\beta = 0.4$, $\sin\theta = 1/\sqrt{2}$ and $M_a = 100\text{GeV}$ in comparison with the one from the generic 2HDM.

a does not mix with the heavy pseudoscalar A ($\sin\theta = 0$): Figure 36 shows the $t\bar{t}$ invariant mass distribution in both cases, showing the peak-dip structure.

While a full study of the sensitivity of this search is not shown in this whitepaper, examples of how its reach changes as a function of the parameters of the 2HDM+a, the $M_{t\bar{t}}$ signal distribution are presented in Fig 37. Larger values of $\tan\beta$ or $\sin\theta$ are expected to yield lower sensitivities to $A \rightarrow t\bar{t}$ significantly while M_a almost only affects the contribution from $a \rightarrow t\bar{t}$, which becomes sizeable if M_a is close to $2M_t$.



(a) $\tan \beta$ dependency with fixed $\sin \theta = 1/\sqrt{2}$ (b) $\sin \theta$ dependency with fixed $\tan \beta = 0.4$ and $M_a = 100\text{GeV}$



(c) M_a dependency with fixed $\tan \beta = 0.4$ and $\sin \theta = 1/\sqrt{2}$

Figure 37: Signal M_{tt} distribution as a function of various model parameters. The value of M_a is fixed at 600GeV .

4.0.4 Four-top final states

The topology involving four top-quarks in the final state is a rare, yet increasingly important signature, which will gain sensitivity and attention with the enlargement of the dataset delivered by the LHC.

In the attempt to perform a first characterization of this final state for this model, we have studied the predicted cross-section for the four top final state of this model for two sets of parameter choices.

In Figure 38a we present the four top cross section for the parameter choices of $\sin \theta = 0.35$, $M_A = M_H = M_{H^\pm} = 600\text{ GeV}$, for an intermediate choice of mass of the light pseudoscalar ($m(a) = 400\text{ GeV}$), as a function of $\tan \beta$.

The total four-top production cross section, which accounts for both SM and new physics (NP) contributions and is indicated as $|SM + NP|^2$ in the legend, is compared with the production cross section contributions separately due to SM and NP terms. This is achieved technically by setting a requirement on the number of QCD and QED vertices

MADGRAPH rule	Legend symbol	Details
$p p \rightarrow t \bar{t} t \bar{t} / a z h1 \text{ QED} \leq 2$	$ SM + NP ^2$	Four-top production including both SM and NP contributions and their interference.
$p p \rightarrow t \bar{t} t \bar{t} / a z h1 \text{ QCD} \leq 2$	$ NP ^2$	Four-top production from NP processes, including interference terms among A, H, a .
$p p \rightarrow t \bar{t} t \bar{t} / a z h1 \text{ QED} \leq 0$	$ SM ^2$	Four-top SM production.

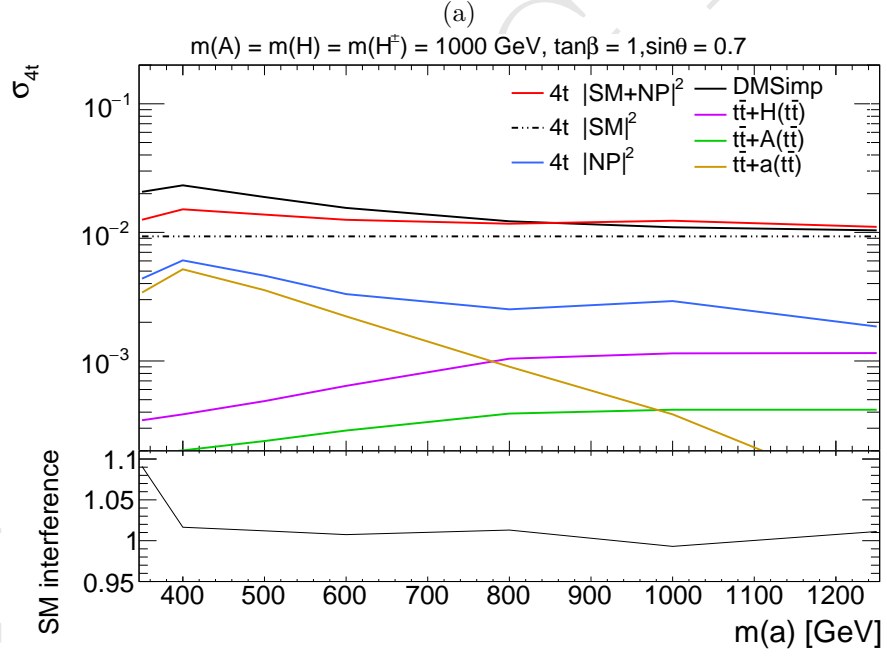
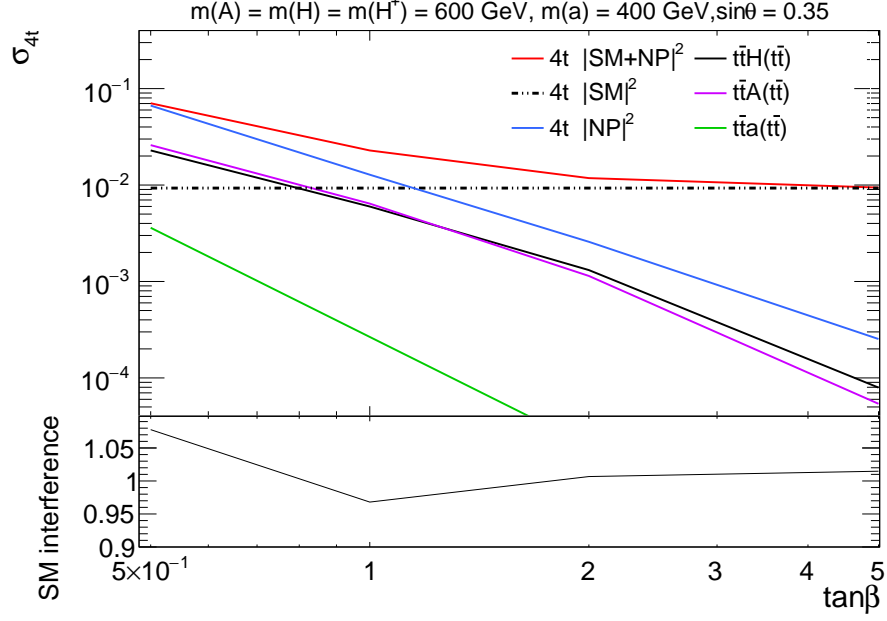
Table 1: Description of the specific MADGRAPH settings used to derive the different curves of Figs 38a and 38b.

in madgraph, as indicated in Table 1. The different contributions from on-shell production of each CP-odd and CP-even mediators associated with a top pair and decaying into a top pair are also shown in the same figure indicated. The dominant contribution is driven by the on-shell production of A and H for all choices of $\tan\beta$ in this benchmark. In the lower panel of Figure 38a, the effect of the interference term between the 2HDM+a and the SM is assessed, and is found to have an impact almost always smaller than 5% on the inclusive cross-section. Note however that the validity of this statement depends on the selection in the experimental analysis.

In Figure 38b we present instead the cross-section study for a different set of parameter choices, for $\sin\theta = \frac{1}{\sqrt{2}}$ and as a function of the light pseudoscalar mass. For these parameter choices, the cross-section is independent of $m(a)$. As it can be observed from the on-shell contribution breakdown, at the low-end of the mass spectrum the $\bar{t}t + a$ production dominates, with a peak at 400 GeV due to the competition between $a \rightarrow \chi\chi$ and $a \rightarrow \bar{t}t$ and the natural decreasing of the cross section with the increase of $m(a)$. The contribution of $\bar{t}t + H$ and $\bar{t}t + A$ processes compensates the latter effect in the higher end of the mass-spectrum, with the turn on starting around 800 GeV due to the competition between $A/H \rightarrow \bar{t}t$ and cascade decays of the heavy higgses into the light pseudoscalar mediator ($A \rightarrow ah/H \rightarrow aZ$). The little bump at 1 TeV is due to interference effects between the three higgs mediators, which are all set to the same mass for this parameter choice. The inclusive production cross-section of the 2HDM+a model is also compared with the one obtained by the DMSimp pseudoscalar implementation. In a similar way as for the previous benchmark points, the impact of the SM interference term on the inclusive cross-section is found to be very small ($< 2\%$), except for $m(a)$ values close to the top threshold.

Finally, in Figure 39 we compare for a small $\tan\beta$ value, the cross section of four-top production from NP processes (see Tab. 1) of benchmarks #3a and #3b.

This cross-section increases for benchmark #3b for increasing $\sin\theta$, as the production mechanism is dominated by $\bar{t}t + a(\bar{t}t)$. A different and more flat trend is instead observed for benchmark #3a, for which the $\sin\theta$ dependence is more complex and driven by the branching ratios of A and H in a top pair, as the $a \rightarrow \bar{t}t$ threshold is closed in this case.



(b)

Figure 38: Four-top cross section study for a subset of the parameter space of benchmark #2 (top) and #3 (bottom). The different Standard Model (SM) and New Physics (NP) contributions with and without interference and the breakdown in terms of on-shell mediator production is presented, following the notation of Table 1.

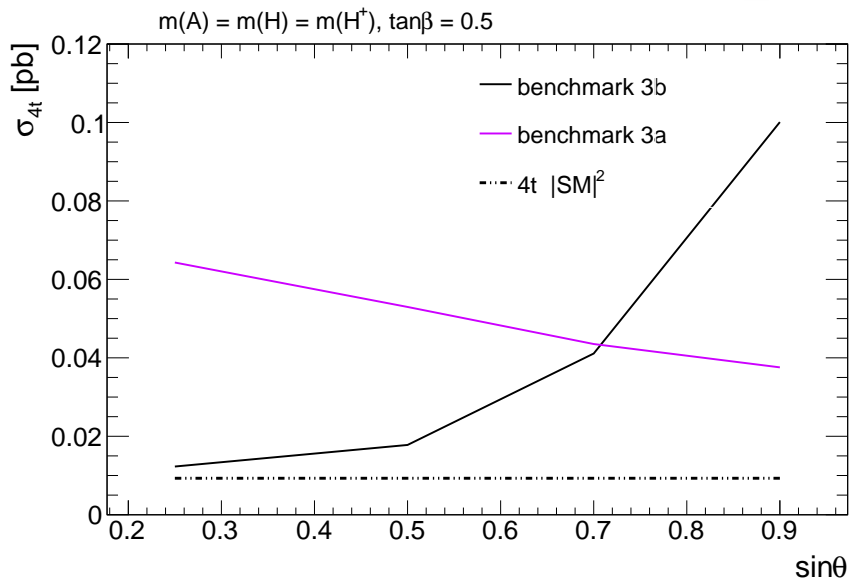


Figure 39: Four-top cross section comparison for benchmarks #3a and #3b. Only NP contribution is presented, following the notation of Table 1.

5 Connection with cosmology

In this section, we check the consistency of the 2HDM+a model as a function of the parameters chosen for the scans with the measured DM relic density, according to the standard thermal relic "freeze-out" scenario. This exercise requires the following assumptions, already described in Ref. [23]:

- The DM annihilation cross section receives only contributions from the interactions of the simplified model, while possible additional degrees of freedom and couplings not included in the model are irrelevant.
- The DM number density in the Universe today is entirely determined by the DM annihilation cross section predicted by the 2HDM+a. In particular, no additional mechanisms exist that enhance or deplete the relic density.

It is important to realize that if one or both of these assumptions are violated there is no strict correlation between the relic density and the strength of mono-X signals. For instance, if DM is overproduced, the relic density can be reduced if the DM has large annihilation cross sections to new hidden sector states. These states might however not be directly accessible at LHC energies. Conversely, the correct DM relic density can still be obtained if the DM is underproduced. For instance, if the hidden sector carries a particle-antiparticle asymmetry (similar to the baryon asymmetry) then this necessarily leads to a larger relic density compared to the conventional freeze-out picture.

5.1 Technical setup

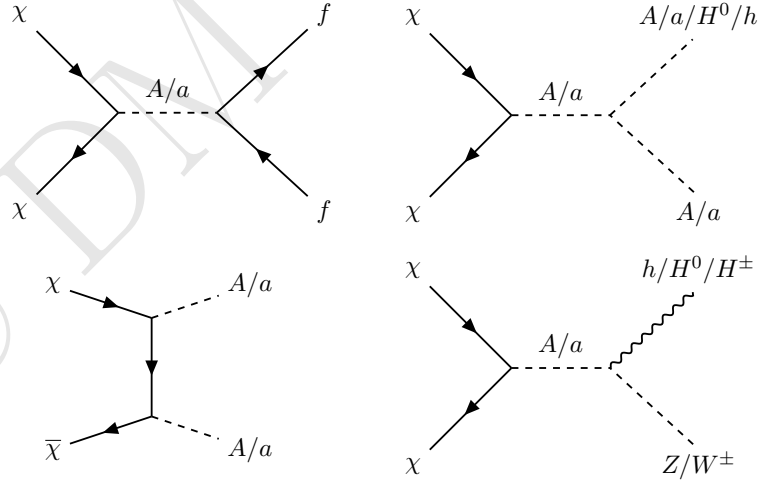


Figure 40: Annihilation diagrams taken into account in the relic density calculation.

The MADDM [24, 25] plugin for MG5_aMC@NLO is used to calculate the present-day relic density for this model. All tree-level annihilation processes are taken into account, and the Yukawa couplings of all fermions are taken to be non-zero. The Feynman diagrams

of annihilation processes taken into account in this calculation are shown in Figure 40. Generally, the annihilation proceeds via single or double s-channel exchange of the pseudoscalars a and A , with subsequent decays. Since MADDM uses only tree-level diagrams, contributions from off-shell pseudoscalars can only be taken into account for the case of single s-channel mediation with direct decay of the pseudoscalars to SM fermions. If the pseudoscalars instead decays to other bosons or if the annihilation proceeds through double s-channel diagrams, the outgoing bosons are taken to be on-shell and their decays are not simulated.

Following section 2, we use the parameter choices $\sin(\theta) = 0.35$, $m_h = 125\text{GeV}$, $g_\chi = 1$, $\lambda_i = 3$ for all scans in this section.

5.2 Results

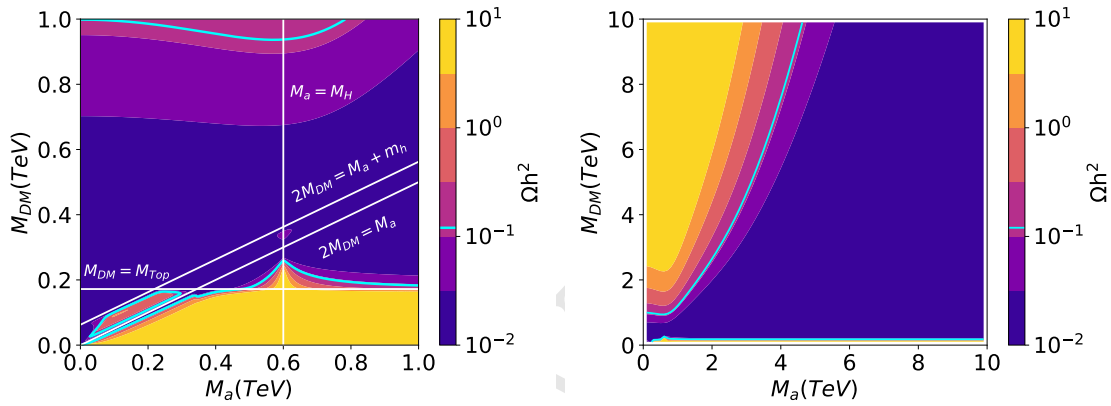


Figure 41: Predicted relic density for a two-dimensional scan of M_χ and M_a . The other parameters of the model remain fixed with $m_H = m_A = m_{H^\pm} = 600\text{ GeV}$ and $\tan\beta = 1$, as well as the default choices described in the text. The color scale indicates the relic density, the cyan solid line shows the observed value of $\Omega h^2 = 0.12$. The color scale is truncated at its ends, i.e. values larger than the maximum or smaller than the minimum are shown in the same color as the maximum/minimum. While the left focuses on the mass region relevant to collider searches, the right panel shows the development of the relic density for a larger mass region.

The relic density is shown for in the M_a - M_χ plane in Figure 41. For small values of M_χ below the mass of the top quark, DM is mostly overabundant. In this regime, annihilation to quarks is suppressed by the small Yukawa couplings of the light fermions. The observed relic density can only be achieved for $M_\chi \approx M_a/2$, where annihilation is resonantly enhanced, or for $M_\chi \approx (M_a + M_h)/2$, close to the threshold for the $\chi\chi \rightarrow ha$ process. Above the top threshold, annihilation into fermions becomes very efficient and DM is underabundant. As M_χ increases further, annihilation via single s-channel diagrams is increasingly suppressed and the relic density rises again. The observed density is produced by this model for $M_\chi \approx 1\text{TeV}$ at low M_a . [The following sentence is being checked with Andreas Albert - would remove] For values of M_a beyond the LHC reach of a few

TeV, the allowed parameter region at the top threshold $M_\chi \approx m_{\text{top}}$ remains independent of the value of M_a , indicating that a DM candidate that is mass degenerate with the top quark cannot be excluded by LHC searches alone.

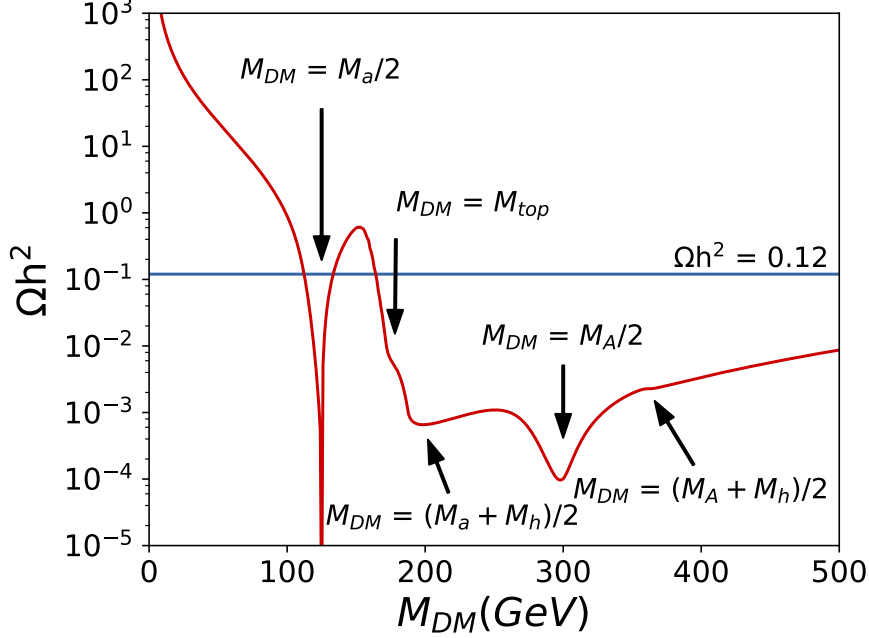


Figure 42: Relic density for a one-dimensional scan of M_χ . The other parameters of the model remain fixed with $m_H = m_A = m_{H^\pm} = 600$ GeV, $M_a = 250$ GeV and $\tan \beta = 1$, as well as the default choices described in the text. Various kinematic thresholds and regions of resonant enhancement are visible. Consistency with the observed value of $\Omega h^2 = 0.12$ is mainly controlled by the resonant enhancement of $\chi\chi \rightarrow a$, as well as the onset of $\chi\chi \rightarrow t\bar{t}$.

The dependence of the relic density on the choice of M_χ is further explored by performing a one-dimensional scan as a function of the DM mass fixing $M_H = M_A = m_{H^\pm} = 600$ GeV, $M_a = 250$ GeV, and shown in Figure 42. The relic density confirms structures corresponding to the previously discussed regions of resonant enhancement and to the kinematic boundaries. Overall, the behavior is dominated by the low- M_χ suppression of the annihilation cross-section, the resonant enhancement at $M_\chi = M_a/2$ and the kinematic top thresholds. Other effects, such as the resonant enhancement of $\chi\chi \rightarrow A$ annihilation are present, but only have small effects.

The relic density values for the M_a - M_A / M_H scan described in section 2 is shown in Figure 43. For the model parameters chosen in this whitepaper, the regions where the model generates a relic density compatible with the measured value are located at relatively small values of $M_a < 30$ GeV or $M_A = M_H = m_{H^\pm} < 30$ GeV, which are already excluded by LHC and LEP searches (see section 4 of Ref. [7]). The cosmological production of DM is largely driven by the choice of M_χ . As shown in subsection 1.2.4, the model kinematics is largely insensitive to this choice if $M_\chi < 2M_a$. Future experimental results that are

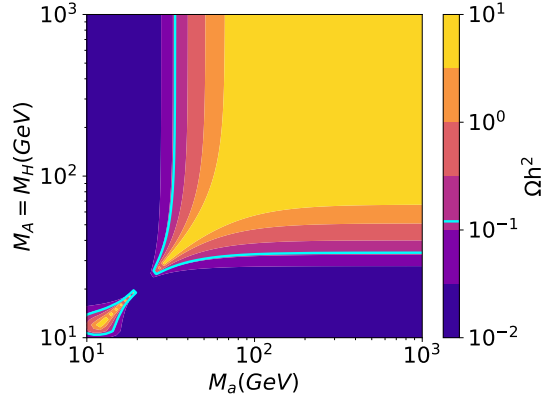


Figure 43: Predicted relic density for a two-dimensional scan of M_a and $M_A = M_H = M_{H^\pm}$. The other parameters of the model remain fixed with $M_\chi = 10$ GeV, $\tan\beta = 1$, $M_H = M_A = m_{H^\pm}$. The color coding is identical to Fig. 41.

sensitive to DM masses around 100 GeV which can yield the measured relic density can still be interpreted by rescaling samples generated according to this parameter scan.

The $\tan\beta$ -dependent scans, as a function of M_a and M_χ , are shown in Fig. 44. The choice of $\tan\beta$ acts as an overall modifier of the annihilation cross-section and thus the relic density, and the effect is largely independent of the choice of M_a and M_χ . For a choice of $\tan\beta \approx 0.6$, the relic density becomes maximal and steadily decreases for larger and smaller values of $\tan\beta$. In the M_χ dependent scan, where M_a is fixed to 250 GeV, the reduction of the relic density at low (≈ 0.1) and high (≈ 3) values of $\tan\beta$ leads to the disappearance of the overabundant island around $M_\chi \approx M_a/2$.

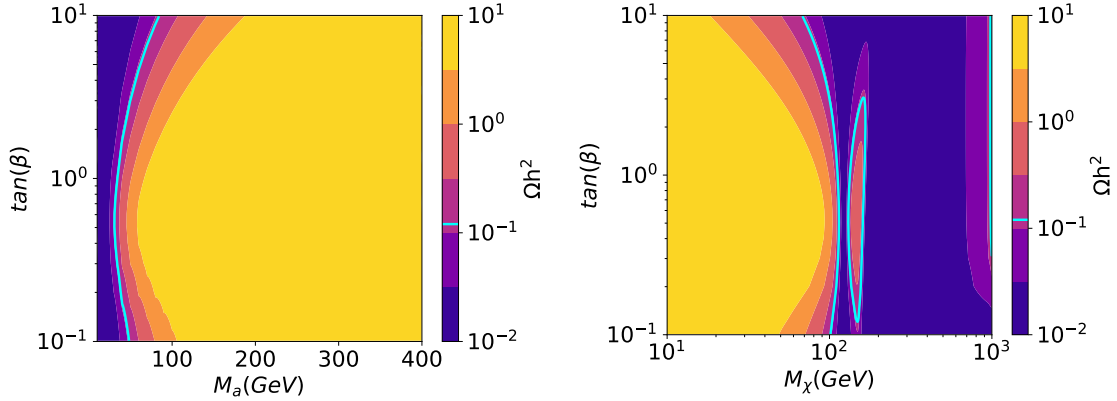


Figure 44: Predicted relic density for a two-dimensional scan of $\tan\beta$ and M_a (left), M_χ (right). In the case of the M_χ (M_a) dependent scan, $M_a = 250$ GeV ($M_\chi = 10$ GeV) is used. The other parameters of the model remain fixed with $m_H = m_A = m_{H^\pm} = 600$ GeV, as well as the default choices described in the text. The color coding is identical to Fig. 41.

6 Conclusions

Appendix

References

- [1] **ATLAS** Collaboration, G. Aad et al., *Observation of a new particle in the search for the Standard Model Higgs boson with the ATLAS detector at the LHC*, *Phys. Lett.* **B716** (2012) 1–29, [[arXiv:1207.7214](#)].
- [2] **CMS** Collaboration, S. Chatrchyan et al., *Observation of a new boson at a mass of 125 GeV with the CMS experiment at the LHC*, *Phys. Lett.* **B716** (2012) 30–61, [[arXiv:1207.7235](#)].
- [3] L. Carpenter, A. DiFranzo, M. Mulhearn, C. Shimmin, S. Tulin, et al., *Mono-Higgs: a new collider probe of dark matter*, *Phys.Rev.* **D89** (2014) 075017, [[arXiv:1312.2592](#)].
- [4] A. A. Petrov and W. Shepherd, *Searching for dark matter at LHC with Mono-Higgs production*, *Phys.Lett.* **B730** (2014) 178–183, [[arXiv:1311.1511](#)].
- [5] **ATLAS** Collaboration, M. Aaboud et al., *Search for Dark Matter Produced in Association with a Higgs Boson Decaying to $b\bar{b}$ using 36 fb⁻¹ of pp collisions at $\sqrt{s} = 13$ TeV with the ATLAS Detector*, [arXiv:1707.01302](#).
- [6] **ATLAS** Collaboration, M. Aaboud et al., *Search for dark matter in association with a Higgs boson decaying to two photons at $\sqrt{s} = 13$ TeV with the ATLAS detector*, [arXiv:1706.03948](#).
- [7] M. Bauer, U. Haisch, and F. Kahlhoefer, *Simplified dark matter models with two Higgs doublets: I. Pseudoscalar mediators*, *JHEP* **05** (2017) 138, [[arXiv:1701.07427](#)].
- [8] J. M. No, *Looking through the pseudoscalar portal into dark matter: Novel mono-Higgs and mono-Z signatures at the LHC*, *Phys. Rev.* **D93** (2016), no. 3 031701, [[arXiv:1509.01110](#)].
- [9] L. M. Carpenter, A. Nelson, C. Shimmin, T. M. Tait, and D. Whiteson, *Collider searches for dark matter in events with a Z boson and missing energy*, [arXiv:1212.3352](#).
- [10] N. F. Bell, J. B. Dent, A. J. Galea, T. D. Jacques, L. M. Krauss, et al., *Searching for dark matter at the LHC with a mono-Z*, *Phys.Rev.* **D86** (2012) 096011, [[arXiv:1209.0231](#)].
- [11] **ATLAS** Collaboration, M. Aaboud et al., *Search for an invisibly decaying Higgs boson or dark matter candidates produced in association with a Z boson in pp collisions at $\sqrt{s} = 13$ TeV with the ATLAS detector*, *Phys. Lett.* **B776** (2018) 318–337, [[arXiv:1708.09624](#)].
- [12] **CMS** Collaboration, A. M. Sirunyan et al., *Search for new physics in events with a leptonically decaying Z boson and a large transverse momentum imbalance in proton-proton collisions at $\sqrt{s} = 13$ TeV*, [arXiv:1711.00431](#).
- [13] U. Haisch, F. Kahlhoefer, and J. Unwin, *The impact of heavy-quark loops on LHC dark matter searches*, *JHEP* **1307** (2013) 125, [[arXiv:1208.4605](#)].
- [14] D. Abercrombie et al., *Dark Matter Benchmark Models for Early LHC Run-2 Searches: Report of the ATLAS/CMS Dark Matter Forum*, [arXiv:1507.00966](#).
- [15] M. Backovic, M. Krämer, F. Maltoni, A. Martini, K. Mawatari, and M. Pellen, *Higher-order QCD predictions for dark matter production at the LHC in simplified models with s-channel mediators*, *Eur. Phys. J.* **C75** (2015), no. 10 482, [[arXiv:1508.05327](#)].

- [16] U. Haisch, P. Pani, and G. Polesello, *Determining the CP nature of spin-0 mediators in associated production of dark matter and $t\bar{t}$ pairs*, [arXiv:1611.09841](#).
- [17] T. Gleisberg, S. Hoeche, F. Krauss, M. Schonherr, S. Schumann, F. Siegert, and J. Winter, *Event generation with SHERPA 1.1*, *JHEP* **02** (2009) 007, [[arXiv:0811.4622](#)].
- [18] G. Cowan, *Discovery sensitivity for a counting experiment with background uncertainty*, tech. rep., Royal Holloway, London, (2012). Available [online] <http://www.pp.rhul.ac.uk/~cowan/stat/medsig/medsigNote.pdf>.
- [19] P. Pani and G. Polesello, *Dark matter production in association with a single top quark at the LHC in a two Higgs doublet model with a pseudoscalar mediator*, [arXiv:1712.03874](#).
- [20] D. Pinna, A. Zucchetta, M. R. Buckley, and F. Canelli, *Single top quarks and dark matter*, *Phys. Rev.* **D96** (2017), no. 3 035031, [[arXiv:1701.05195](#)].
- [21] M. Carena and Z. Liu, *Challenges and opportunities for heavy scalar searches in the $t\bar{t}$ channel at the LHC*, *JHEP* **11** (2016) 159, [[arXiv:1608.07282](#)].
- [22] **ATLAS** Collaboration, M. Aaboud et al., *Search for Heavy Higgs Bosons A/H Decaying to a Top Quark Pair in pp Collisions at $\sqrt{s} = 8$ TeV with the ATLAS Detector*, *Phys. Rev. Lett.* **119** (2017), no. 19 191803, [[arXiv:1707.06025](#)].
- [23] A. Albert et al., *Recommendations of the LHC Dark Matter Working Group: Comparing LHC searches for heavy mediators of dark matter production in visible and invisible decay channels*, [arXiv:1703.05703](#).
- [24] M. Backovic, K. Kong, and M. McCaskey, *MadDM v.1.0: Computation of Dark Matter Relic Abundance Using MadGraph5*, *Physics of the Dark Universe* **5-6** (2014) 18–28, [[arXiv:1308.4955](#)].
- [25] M. Backovic, A. Martini, O. Mattelaer, K. Kong, and G. Mohlabeng, *Direct Detection of Dark Matter with MadDM v.2.0*, *Phys. Dark Univ.* **9-10** (2015) 37–50, [[arXiv:1505.04190](#)].